Washington University School of Medicine
Digital Commons@Becker

Open Access Publications

3-23-2021

EPB41L5 controls podocyte extracellular matrix assembly by adhesome-dependent force transmission

Jasmin I Maier

Manuel Rogg

Martin Helmstädter

Alena Sammarco

Oliver Schilling

See next page for additional authors

Follow this and additional works at: https://digitalcommons.wustl.edu/open_access_pubs

Authors

Jasmin I Maier, Manuel Rogg, Martin Helmstädter, Alena Sammarco, Oliver Schilling, Benedikt Sabass, Jeffrey H Miner, Jörn Dengjel, Gerd Walz, Martin Werner, Tobias B Huber, and Christoph Schell

Cell Reports

Article

EPB41L5 controls podocyte extracellular matrix assembly by adhesome-dependent force transmission

Graphical Abstract

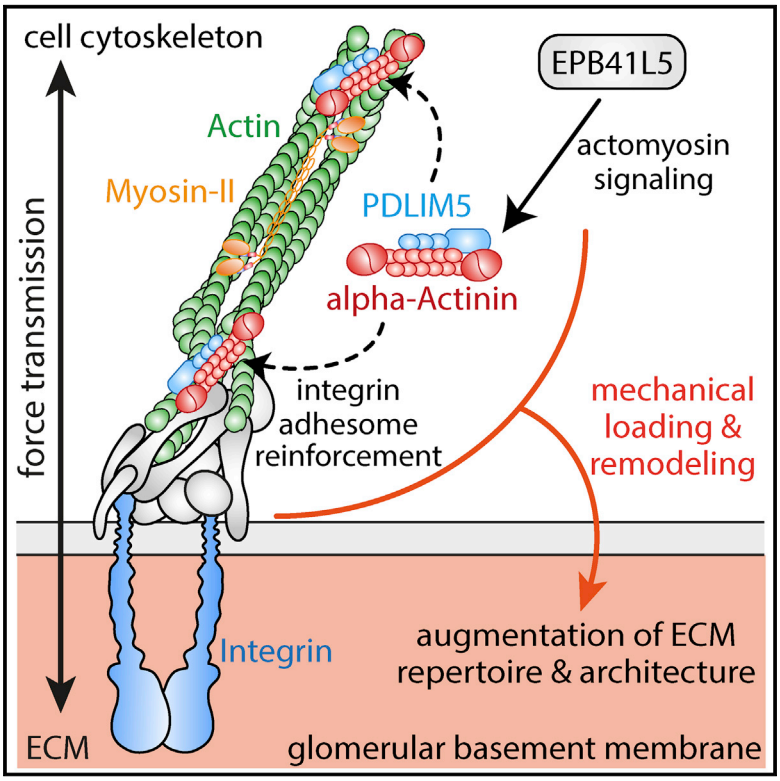

Highlights

- EPB41L5 modulates the structure of the glomerular basement membrane
- EPB41L5 determines the repertoire and architecture of podocyte-derived ECM
- Force transmission by IACs is required for sufficient ECM synthesis of podocytes
- Recruitment of PDLIM5 and ACTN4 to IACs controls force transmission

Authors

Jasmin I. Maier, Manuel Rogg, Martin Helmstädter, ..., Martin Werner, Tobias B. Huber, Christoph Schell

Correspondence

christoph.schell@uniklinik-freiburg.de

In brief

Maier et al. describe an EPB41L5-controlled mechanism for how force transmission by integrin-based adhesion complexes (IACs) controls the structural integrity and function of the glomerular basement membrane (GBM).

Maier et al., 2021, Cell Reports *34*, 108883
March 23, 2021 © 2021 The Author(s).
https://doi.org/10.1016/j.celrep.2021.108883

CellPress

Cell Reports

CellPress
OPEN ACCESS

Article

EPB41L5 controls podocyte extracellular matrix assembly by adhesome-dependent force transmission

Jasmin I. Maier,[1,8] Manuel Rogg,[1,8] Martin Helmstädter,[2] Alena Sammarco,[1] Oliver Schilling,[1] Benedikt Sabass,[3] Jeffrey H. Miner,[4] Jörn Dengjel,[5] Gerd Walz,[2] Martin Werner,[1] Tobias B. Huber,[6] and Christoph Schell[1,7,9,*]

[1]Institute of Surgical Pathology, Faculty of Medicine, University Medical Center Freiburg, Freiburg 79106, Germany
[2]Department of Medicine IV, Faculty of Medicine, University Medical Center Freiburg, Freiburg 79106, Germany
[3]Bacteriology and Mycology, Institute for Infectious Diseases and Zoonoses, Department of Veterinary Sciences, LMU Munich, 80539 Munich, Germany
[4]Division of Nephrology, Washington University School of Medicine, St. Louis, MO 63110, USA
[5]Department of Biology, University of Fribourg, Fribourg 1700, Switzerland
[6]III. Department of Medicine, University Medical Center Hamburg-Eppendorf, Hamburg 20246, Germany
[7]Berta-Ottenstein Program, Medical Faculty, University Medical Center, Freiburg 79106, Germany
[8]These authors contributed equally
[9]Lead contact
*Correspondence: christoph.schell@uniklinik-freiburg.de
https://doi.org/10.1016/j.celrep.2021.108883

SUMMARY

The integrity of the kidney filtration barrier essentially relies on the balanced interplay of podocytes and the glomerular basement membrane (GBM). Here, we show by analysis of *in vitro* and *in vivo* models that a loss of the podocyte-specific FERM-domain protein EPB41L5 results in impaired extracellular matrix (ECM) assembly. By using quantitative proteomics analysis of the secretome and matrisome, we demonstrate a shift in ECM composition characterized by diminished deposition of core GBM components, such as LAMA5. Integrin adhesome proteomics reveals that EPB41L5 recruits PDLIM5 and ACTN4 to integrin adhesion complexes (IACs). Consecutively, EPB41L5 knockout podocytes show insufficient maturation of integrin adhesion sites, which translates into impaired force transmission and ECM assembly. These observations build the framework for a model in which EPB41L5 functions as a cell-type-specific regulator of the podocyte adhesome and controls a localized adaptive module in order to prevent podocyte detachment and thereby ensures GBM integrity.

INTRODUCTION

Cell-matrix interactions are essential for a plethora of biological processes ranging from embryogenesis to tumor metastasis (Kechagia et al., 2019; Winograd-Katz et al., 2014). Efficient linkage between extracellular matrix (ECM) components and the intracellular actin cytoskeleton is established by integrin heterodimer receptors. On the cytoplasmic part of these receptors, diverse linker, adaptor, and kinase proteins are recruited, resulting in a multiprotein complex commonly termed the integrin adhesion complex (IAC) or integrin adhesome (Winograd-Katz et al., 2014). Based on the molecular repertoire, IACs enable bidirectional signaling (inside-out, outside-in), influencing intracellular processes as well as interaction with the extracellular milieu. Despite a multitude of studies elucidating the molecular composition and signaling pathways of the IAC in a ligand-dependent manner, knowledge is limited whether and how IACs reciprocally shape their extracellular environment in a cell-type-specific manner.

The integrity of the kidney filtration barrier relies on the interplay of glomerular endothelial cells, specialized epithelial cells (podocytes), and a unique basement membrane (BM) (Grahammer et al., 2013). Within this three-layered filter, the glomerular BM (GBM) is formed by a fusion of initially independent BMs produced by epithelial and endothelial cells during glomerular development and maturation (Chew and Lennon, 2018). The mature GBM is composed of distinct ECM constituents, in which specialized networks of collagen type IV ($\alpha3\alpha4\alpha5$) and laminin-521 serve as essential scaffold components, as evidenced by genetic diseases and elegant *in vivo* studies (*COL4A3/A4/A5*, Alport syndrome; and *LAMB2*, Pierson syndrome (Chew and Lennon, 2018; Suh and Miner, 2013; Suleiman et al., 2013). Not only hereditary syndromes but also acquired diseases such as diabetic nephropathy or even kidney transplant glomerulopathy affect the integrity of the GBM by altering structure and composition (Zhang et al., 2018). There is still an ongoing debate to what extent the GBM itself impacts the properties of the kidney filtration barrier (Suh and Miner, 2013), but it is clear that its structure

This is an open access article under the CC BY-NC-ND license (http://creativecommons.org/licenses/by-nc-nd/4.0/).

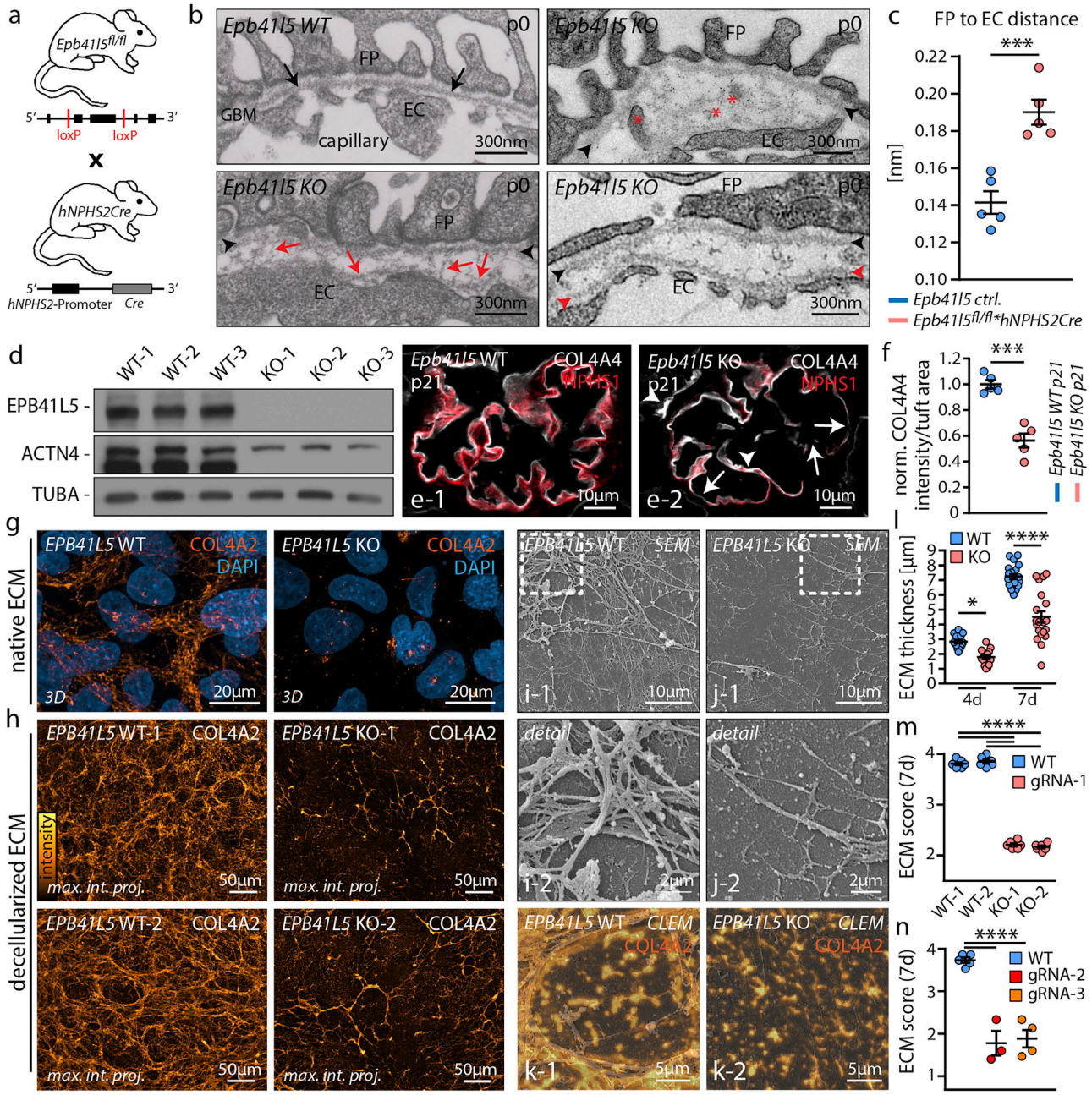

Figure 1. The podocyte-enriched FERM-domain protein EPB41L5 controls GBM development *in vivo* and extracellular matrix synthesis *in vitro*

(A) Schematic illustrating the generation of a podocyte-specific *Epb41l5* KO mouse model by using *hNPHS2Cre*.

(B) Ultrastructural analysis shows impaired BM fusion and altered internal structure of the GBM (red asterisks indicate nodular matrix fragments; red arrows mark splitting of the GBM; black and red arrowheads indicate podocyte and endothelial BM, respectively; FP, foot process; EC, endothelial cell; GBM, glomerular basement membrane).

(C) FP to EC distance quantification shows increased GBM thickness in *Epb41l5* KO mice at P0 (each dot indicates one animal; 1–6 glomeruli per individual mouse were analyzed; ***$p < 0.001$).

(D) Glomeruli from *Epb41l5*hNPHS2Cre* KO and WT mice were isolated at P21. Western blot analysis for EPB41L5, ACTN4, and TUBA confirms loss of EPB41L5.

(E and F) Immunofluorescence analysis of glomerular COL4A4 expression demonstrates reduced expression levels in KO mice at P21 (each dot indicates 1 individual animal; 21–57 glomeruli per mouse were analyzed; ***$p < 0.001$; white arrows highlight areas of decreased COL4A4 GBM staining, whereas white arrowheads mark areas with accumulations of COL4A4 staining intensities).

(G–K) 3D reconstruction of matrix networks highlights decreased collagen IV fiber density in cellular-derived matrices from *EPB41L5* KO podocytes. Multimodal morphological analysis (including immunofluorescence, scanning electron microscopy, as well as CLEM) of decellularized ECM demonstrates decreased levels

(legend continued on next page)

unequivocally provides the basis for efficient podocyte adhesion. Podocytes are post-mitotic cells with only a limited capacity for regeneration and form the outer layer of the kidney filtration barrier by tightly covering glomerular capillaries with specialized cellular protrusions (commonly termed as foot processes). These foot processes establish and maintain podocyte adhesion to the GBM against physical filtration forces relying on a specialized cytoskeleton and adhesion machinery (Lennon et al., 2014b). The relevance of efficient podocyte adhesion is well documented for acquired as well as hereditary forms of glomerulosclerosis (e.g., *Itga3* mutations; Nicolaou et al., 2012; Kreidberg et al., 1996). Podocytes are anchored to the GBM by the integrin adhesome, e.g., by the laminin receptor integrin $\alpha3\beta1$ to establish a tight linkage toward the actin cytoskeleton (e.g., via Talin-1 [TLN1], Kindlin-2 [*FERMT2*] and α-*Actinin-4* [*ACTN4*]). Remarkably, a series of *in vivo* knockout (KO) models proved the indispensable role of IAC components and revealed their involvement in force sensing and transduction (Kreidberg et al., 1996; Tian et al., 2014; Yasuda-Yamahara et al., 2018a; Rogg et al., 2021). Furthermore, recent proteomic studies demonstrated a cell-type-specific molecular composition of the podocyte IAC and GBM (Schell et al., 2017; Randles et al., 2020; Byron et al., 2014; Lennon et al., 2014a). However, it still remains unclear whether podocyte-specific components of the IAC contribute to the generation and assembly of the unique GBM and if reciprocal interactions between these two compartments influence the functional integrity of the filtration barrier.

We have recently identified the FERM-domain protein EPB41L5 as a podocyte-specific regulator of integrin adhesion formation by recruiting ARHGEF18 and activating RHOA-ROCK1/2-actomyosin signaling under dynamic conditions (Schell et al., 2017). Based on the analysis of *in vivo* as well as *in vitro* systems, we describe here the impact of EPB41L5 on the podocyte secretome, matrisome, and GBM *in vivo*. Our observations imply that EPB41L5 serves as a modulator of force-dependent IAC maturation by adhesome modulations for ACTN4 and PDLIM5, resulting in ECM remodeling and shaping.

RESULTS

The podocyte-enriched FERM-domain protein EPB41L5 controls ECM synthesis *in vitro* and GBM development *in vivo*

To preserve the integrity of the glomerular filtration barrier, podocytes rely on a complex machinery to maintain their adhesion to the GBM. We recently identified the FERM-domain protein EPB41L5 as a core component of the podocyte integrin adhesome (Figure S1; Schell et al., 2017; Rinschen et al., 2018). To explore the functional relevance of EPB41L5 for GBM integrity, we generated a podocyte-specific conditional KO mouse model by using the *Epb41l5*$^{fl/fl}$*hNPHS2Cre allele as previously reported (Figure 1A; Figure S1) (Schell et al., 2017). Ultrastructural analysis of respective *Epb41l5* KO animals by transmission electron microscopy (TEM) demonstrated impaired fusion of endothelial and epithelial BM and pathological remodeling of the GBM at post-natal day 0 (P0) and P7 (Figures 1B and 1C; Figure S2), indicating impaired GBM development *in vivo*. Moreover, loss of EPB41L5 led to a successive depletion of GBM-specific collagen IV ($\alpha3/\alpha4\alpha/5$) network and to aberrant expression of developmental BM components like LAMB1 and collagen IV $\alpha1/2$ (Figures 1D–1F; Figure S3). To test the specificity and functional relevance of EPB41L5 for ECM synthesis, we analyzed CRISPR-Cas9-genome-edited *EPB41L5* KO clones of human immortalized podocytes *in vitro*. We used two well-characterized *EPB41L5* KO clones to synthesize podocyte-derived matrices and combined this method with efficient podocyte decellularization for further downstream applications (Schell et al., 2017; Kaukonen et al., 2017). Immunofluorescence analysis for collagen IV (COL4A2) revealed a decreased assembly of collagen IV fibers and structural alterations characterized by an overall decreased filament density due to the loss of *EPB41L5* (Figures 1G and 1H). These observations were furthermore corroborated by scanning electron microscopy, demonstrating a general reduction of ECM network density in respective KO podocytes (Figure 1I and 1J). Moreover, correlative light and electron microscopy (CLEM) of COL4A2 showed localization to the majority of ECM fibers, indirectly validating COL4A2 as a sufficient marker for an altered ECM/cell-derived matrix (CDM) structure (Figure 1K). Analysis of an additional seven individual *EPB41L5* KO clones generated from two additional guide RNAs (gRNAs) and *EPB41L5* rescue experiments substantiated these findings (Figure 1N; Figure S4).

EPB41L5 differentially impacts protein profiles of the podocyte secretome and matrisome

To characterize *EPB41L5*-dependent ECM modification on a global and molecular level, we isolated the soluble (conditioned media) and insoluble (CDM) extracellular fraction and performed quantitative mass spectrometry (Figure 2A). By using this approach, we identified 2,155 proteins within the secretome (soluble fraction) and 402 proteins within the matrisome (insoluble fraction). Label-free quantification of secretome proteins and quantitative SILAC (stable isotope labeling with amino acids) based matrisome analysis revealed distinct alterations of the podocyte secretome and matrisome composition due to the loss of *EPB41L5* (Figures 2B and 2C; Table S1). Filtering these datasets by using a consensus ECM protein database (The Matrisome Project) not only validated the efficient isolation of ECM proteins

of collagen IV network density in *EPB41L5* KO matrices (maximum intensity projection of COL4A2 immunofluorescence; boxed areas indicate zoomed-in details; fluorescence intensities were transformed to gold LUT, as indicated by intensity charts).

(L) Quantification of ECM thickness synthesized over 4 and 7 days (scatterplots indicate individual measurements; 15 per genotype at 4 days and 20 at 7 days; ****$p < 0.0001$).

(M and N) Semiquantitative ECM scoring (grading fibrillary COL4A2 network density and connectivity) demonstrates impaired network integrity due to loss of EPB41L5 (please see STAR Methods for detailed criteria for 5-tier grade ECM scoring and Figure S4 for exemplary images illustrating scoring; quantification for 9 individual CRISPR/Cas9 *EPB41L5* KO clones, derived from 3 independent gRNAs, as well as 3 corresponding WT controls; ****$p < 0.0001$). Data are represented as mean ± SEM.

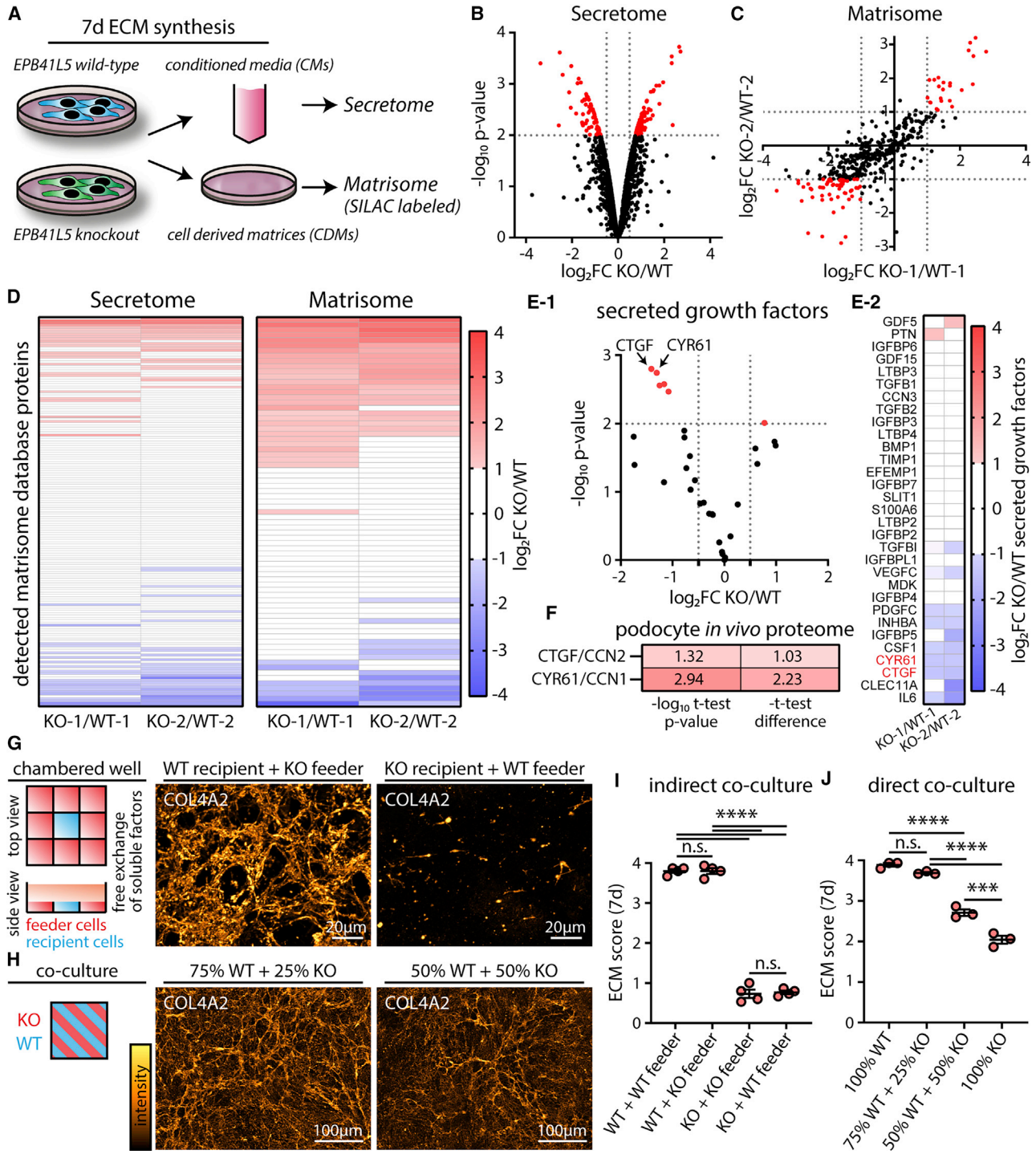

Figure 2. EPB41L5 differentially impacts protein profiles of the podocyte secretome and matrisome

(A) Schematic depicting the generation of EPB41L5-dependent secretome and matrisome preparations for further quantitative mass spectrometry (MS) analysis.

(B and C) Scatterplots indicating detected proteins from MS analysis (2,155 secretome and 402 matrisome proteins). Significantly regulated proteins are highlighted in red ($p < 0.01$ for secretome proteins and $\log_2$ fold change [FC] > 1 or < −1 in both SILAC-labeled replicates of matrisome proteins; see also Table S1).

(D) Heatmaps depicting $\log_2$FC for consensus ECM proteins detected by MS analysis.

(E) Detailed analysis of the secretome dataset shows significantly changed patterns for secreted growth factors (e.g., downregulation of CTGF and CYR61) due to the loss of EPB41L5 (red dots indicate $p < 0.01$).

(F) Comparative re-analysis with murine podocyte proteome (Rinschen et al., 2018) confirms the podocyte-specific expression of CTGF (CCN2) and CYR61 (CCN1) *in vivo*.

(legend continued on next page)

but also demonstrated marked regulation of core matrisome proteins (Figure 2D; Naba et al., 2016). Detailed analysis of the secretome dataset indicated alterations in the pattern of secreted growth factors, suggesting a potential involvement of *EPB41L5* in intraglomerular signaling processes (Figure 2E). In particular, CYR61 (CCN1) and CTGF (CCN2), two well-known soluble factors affecting endothelial cell functions, were significantly decreased by the loss of *EPB41L5* and were identified as specifically expressed by podocytes *in vivo* (Figure 2F; Brigstock, 2002; Sawai et al., 2007; Toda et al., 2018). Based on these analyses, we reasoned that EPB41L5-dependent changes in the secretory repertoire (e.g., growth factors or matrix-metalloproteinases) might be causative for the observed structural ECM phenotypes. To examine whether soluble factors alter GBM composition after *EPB41L5* depletion, we performed indirect and direct co-culture assays with *EPB41L5* WT and KO podocytes. However, the presence of *EPB41L5* KO podocytes or conditioned medium did not significantly influence the structural ECM phenotype of WT podocytes, and the correlation of secretome and matrisome datasets did not reveal a direct relation for altered abundances of soluble and insoluble ECM proteins on a global level (Figures 2G–2I; Figure S5). Moreover, the application of a broad-spectrum matrix metalloproteinase (MMP) inhibitor did not affect *EPB41L5*-dependent structural ECM phenotypes. Therefore, we conclude that the observed structural ECM phenotype of *EPB41L5* KO podocytes is not mediated by soluble factors

EPB41L5 facilitates incorporation of secreted proteins into filamentous ECM

We next examined whether cell-inherent defects are causative for the observed changes of the GBM after elimination of *EPB41L5*. The integrity of the GBM relies on its unique molecular composition of the collagen-IV-linker-laminin complex. Moreover, correct incorporation of laminin-521 and -511 chains appears to be one main determinant for physiological integrin-receptor-mediated GBM signaling *in vivo* (Suleiman et al., 2013). An analysis of core GBM components within the secretome and matrisome datasets revealed distinct alterations due to the loss of EPB41L5 (Figures 3A–3D). In line with our initial observations of a low filament density CDM in *EPB41L5* KO podocytes, further characterization of core components within the collagen-IV-linker-laminin complex demonstrated an almost complete loss of these proteins from the insoluble ECM (CDM) (Figure 3D). Most of these proteins were enriched (e.g., laminin-521 and Nidogen-1/2), unaffected (e.g., Agrin), or only modestly decreased (collagen IV) in the soluble extracellular fraction (secretome) (Figures 3B and 3D; Figure S5). Because the overall secretory capacity of *EPB41L5* KO podocytes is unchanged (Figure 3C), these observations imply a defective incorporation of the collagen-IV-linker-laminin complex into insoluble ECM (e.g., filamentous) in *EPB41L5* KO podocytes. One potential explanation for this phenomenon is provided by a model of collagen-IV-dependent stabilization of the collagen-IV-linker-laminin complex, for which polymerized collagen IV is required to establish a stable matrix scaffold for further incorporation of laminin-521/-511 by linker proteins (Mouw et al., 2014). As expected, levels of polymerized collagen IV were significantly reduced in KO-derived matrices (Figure 3E). Furthermore, immunofluorescence (IF)-based analysis of wild-type (WT)- and KO-derived matrices for LAMA5 and LAMC1 confirmed decreased laminin incorporation into KO-derived matrices and revealed a predominant recruitment of laminin to filamentous collagen IV (Figures 3F and 3G; Figure S6). Based on these observations, the inverse abundance of laminin-521/-511 within the soluble and insoluble ECM fraction (i.e., secretome and matrisome) might be attributed to a defective assembly of collagen IV networks. Together with the observed GBM alterations for collagen IV α3/α4/α5 networks in *Epb41l5* KO mice (Figure 1), these data indicate that *EPB41L5* serves as a regulator of molecular ECM composition, stabilizing the collagen-IV-linker-laminin complex. Hereditary laminino- and collagenopathies (e.g., Alport syndrome) revealed that podocytes rely on physiological GBM collagen IV and laminin networks (Funk et al., 2018). We reasoned that the *EPB41L5*-dependent matrisome might influence the functional capacities of podocytes. Therefore, we performed cell adhesion assays to evaluate ECM ligand-to-integrin receptor affinity and binding (Figures 3H–3L). These assays demonstrated overall reduced integrin receptor binding when WT podocytes were exposed to CDMs derived from *EPB41L5* KO cells (Figures 3I and 3J). Exogenous enrichment of respective KO CDMs with either non-filamentous collagen I or laminin-521 was sufficient to ameliorate this phenotype (Figures 3K and 3L). This result indicates that a diminished abundance of specific integrin ligands is the underlying mechanism for decreased adhesion properties. Furthermore, podocytes showed an overt morphological simplification on KO CDMs characterized by decreased generation of cellular protrusions, increased myosin II activation levels, and nuclear YAP/TAZ translocation (Figures S6C–S6J). Thus, *EPB41L5*-dependent ECM remodeling appears to be a prerequisite for efficient and balanced outside-in signaling in podocytes.

EPB41L5 controls IAC function

Integrin receptor function is a major determinant for physiological BM signaling and remodeling (Jayadev et al., 2019; Hohenester and Yurchenco, 2013; Humphrey et al., 2014). ECM synthesis and reorganization is accepted as a continuous and long-lasting biological process. Based on these observations, we reasoned that *EPB41L5* might modulate and fine-tune already established IACs, thereby impacting podocyte ECM remodeling. To evaluate integrin function, we performed cell adhesion assays on defined integrin ligands by using *EPB41L5* WT

(G) Indirect co-culturing of WT and *EPB41L5* KO podocytes allowing for free exchange of soluble factors does not alter ECM structure, as assessed by staining for COL4A2 networks.
(H) Direct co-culturing (in defined ratios of WT and KO cells) demonstrates a linear correlation between the loss of EPB41L5 and only minimal ECM network density (transformation to gold LUT as indicated; maximum intensity projections [MIPs] for COL4A2).
(I and J) Quantification of co-culture experiments by ECM scoring (3 independent experiments and 1–2 replicates per clone and experiment were analyzed; ns, non-significant; ****$p < 0.0001$). Data are represented as mean ± SEM

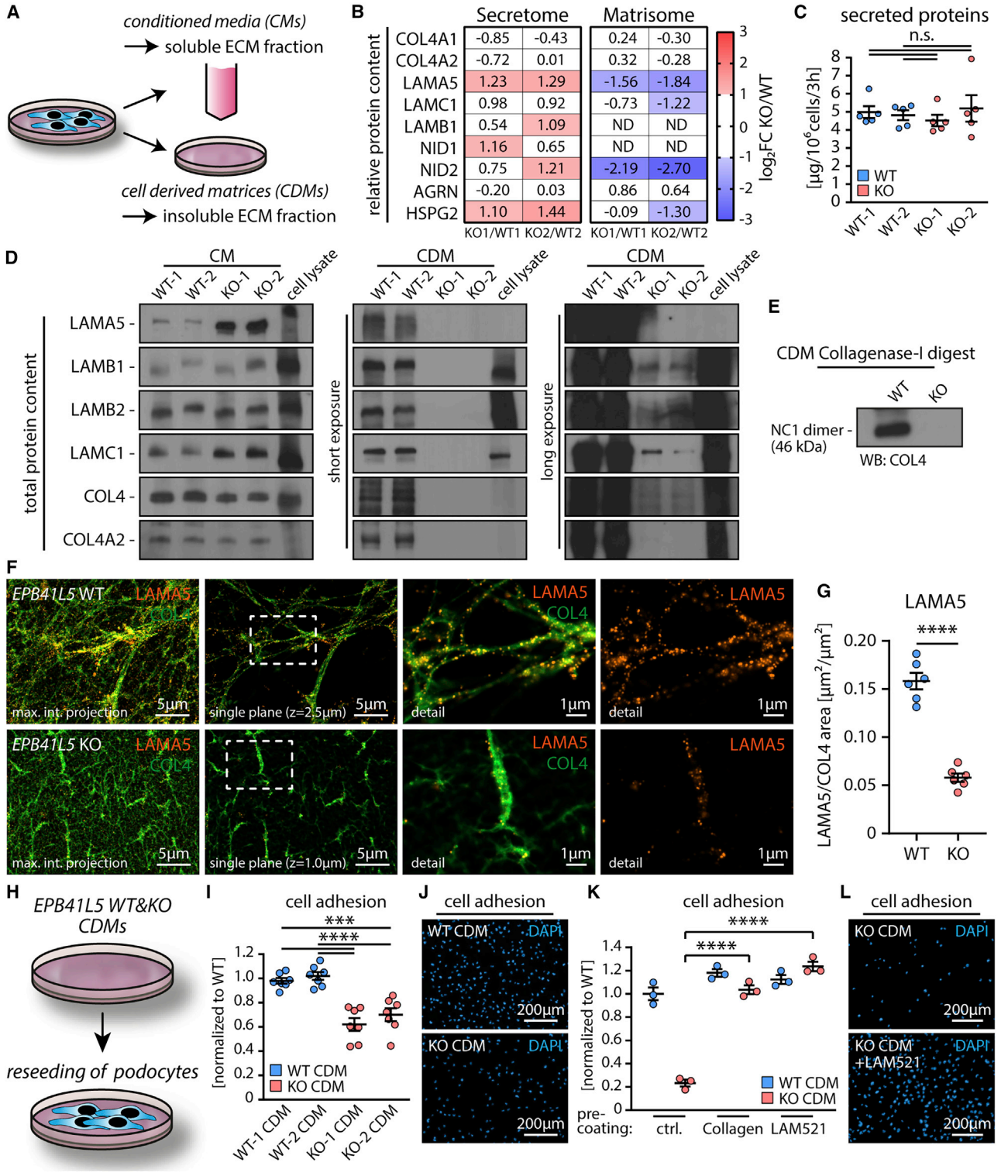

Figure 3. EPB41L5 facilitates incorporation of secreted proteins into filamentous ECM

(A) Schematic depicting the generation of soluble (secretome/conditioned medium [CM]) and insoluble (matrisome/cell-derived matrices [CDMs]) ECM fractions.

(B) Comparative analysis of EPB41L5-dependent secretome and matrisome datasets shows an inverse relationship for core proteins of the GBM (secretome and matrisome samples are adjusted to relative protein content for proteomic analysis).

(legend continued on next page)

and KO podocytes (Figures 4A and 4B). These experiments demonstrated an impaired ligand affinity of *EPB41L5* KO podocytes on all tested ligands, but it was even more pronounced for collagen I and collagen IV. Morphometric evaluation of IACs on collagen-IV-coated substrates showed a significant decrease in IAC density with a loss of more matured adhesion classes (Figures 4C–4E). Concomitantly, mean adhesion size and relative distribution of adhesion numbers per size class were overall shifted to smaller adhesions in *EPB41L5* KO podocytes (Figures 4F and 4G). Of note, individual adhesion morphology and recruitment of mechano-adapters like Zyxin to already matured adhesion classes were unaffected (Figures 4H and 4I). However, the total level of adhesion-bound Zyxin per cell was drastically decreased in KO podocytes, reflecting the significant loss of matured and force-dependent adhesions (Figures 4J and 4K). These data indicate an intricate interdependency between impaired IAC maturation, reduced ligand binding, and mechano-signaling, which critically relies on EPB41L5 function in podocytes.

EPB41L5 controls podocyte matrix remodeling by force-dependent adhesion maturation

Podocytes are constantly exposed to mechano-physical forces such as glomerular filtration and matrix rigidity of the GBM (Endlich et al., 2017). In general, external substrate forces are transduced by integrin adhesion sites and result in the recruitment of cytoskeletal linker and adaptor proteins. This process leads to reinforcement of integrin-cytoskeleton linkage and initiates adhesion site stabilization and maturation (Kechagia et al., 2019). To examine force-dependent adhesion maturation, we analyzed substrate-rigidity-dependent IAC formation in podocytes. Morphometric analysis of WT and *EPB41L5* KO podocytes on either stiff or soft substrates demonstrated an overall impaired adaptation of IACs in KO cells. Not only total adhesion area but also parameters such as adhesion density and IAC size on stiff substrates were decreased in *EPB41L5* KO podocytes (Figures 5A–5D). Moreover, the direct measurement of exerted forces using traction force microscopy revealed reduced traction and strain energies in *EPB41L5* KO podocytes (Figures 5E and 5F). IACs connect the ECM and the actin cytoskeleton, allowing bidirectional transmission of extra- and intracellular forces (Kechagia et al., 2019). Therefore, we speculated that this impaired transmission of forces by *EPB41L5* KO cells might also translate into diminished remodeling of the underlying matrix substratum. In fact, analyzing the remodeling of collagen I fibers revealed less compaction of collagen fibers by KO podocytes, indicating reduced force transmission to the collagen substrate (Figure 5G). Based on these observations, we hypothesized that defective mechano-linkage and force transduction to the ECM by IACs are responsible for the structural ECM phenotype in response to the loss of EPB41L5. To evaluate this hypothesis, we analyzed extracellular matrices derived from two independent models by directly targeting either the structural composition of IACs or the inherent actomyosin contractile machinery by chemical inhibition. FERMT2 is a well-known linker protein at integrin adhesions mediating efficient force transduction (Sun et al., 2019). CRISPR-Cas9-engineered *FERMT2* KO podocytes showed a drastic reduction in ECM generation (Figures 5H and 5I). Inhibition of inherent intracellular contractility by manipulation of the RhoA/ROCK/actomyosin signaling pathway by Y27632 led to a similar phenotype, characterized by only scarce and unorganized deposition of collagen IV and laminin networks (Figures 5J and 5K; Figure S7). Together, these observations suggest that balanced IAC maturation and consecutive force transmission are prerequisites for efficient matrix assembly and structure.

ACTN4 and PDLIM5 recruitment to the integrin adhesome is promoted by EPB41L5

To elucidate potential mechanisms for how EPB41L5 modulates IAC maturation, we performed SILAC-based integrin adhesome proteomics. Interestingly, an analysis of this EPB41L5-modulated adhesome showed a marked enrichment of proteins commonly attributed to the cytoskeleton-IAC interface (Figure 6A). Further classification of detected proteins demonstrated that the majority of these enriched proteins are recruited to the adhesome in a myosin-II- and LIM-domain-dependent manner (Schiller et al., 2011; Kuo et al., 2011). EPB41L5 promoted not only the recruitment of well-described mechano-adapters like ZYX but also of ACTN4 and PDLIM5. These observations were further corroborated by IF studies showing decreased differential recruitment levels of ZYX, ACTN4, and PDLIM5 to integrin adhesion sites in an EPB41L5-dependent mode (Figures 4J, 4K, 6B, and 6C). Moreover, modulation of substrate stiffness or titrating actomyosin contractility of podocytes by Y27632 treatment demonstrated that recruitment of PDLIM5 and ACTN4 to IACs occurs in a mechanosensitive mode (Figures 6D and 6E). Recently, we described EPB41L5 as a regulator of the RhoA/ROCK/actomyosin pathway by directly interacting

(C) The overall secretory capacity of podocytes is not altered due to the loss of EPB41L5 (3 independent experiments and 1–2 replicates per clone and experiment were analyzed).
(D) Western blot experiments of soluble and insoluble ECM fractions confirm proteomic analysis and demonstrate diminished incorporation of laminins and collagens in CDMs of *EPB41L5* KO cells (samples were not adjusted to relative protein content for western blot analysis, revealing total protein abundances).
(E) Western blot analysis of collagenase-I-digested CDMs shows decreased abundance of crosslinked collagen IV (COL4) in matrices derived from KO cells, as indicated by collagen IV NC1 domain dimers.
(F) Immunofluorescence analysis of collagen IV and laminin chains confirms decreased incorporation of COL4 and LAMA5 in filamentous ECM of *EPB41L5* KO podocytes (overviews). Laminin was predominantly detected attached to collagen IV filaments (boxed regions indicate zoomed-in detail).
(G) Quantification of LAMA5 recruitment to collagen IV fibers (dots indicate analyzed maximum intensity projections of 88- × 66-μm micrographs; ****$p < 0.0001$).
(H) Schematic depicting reseeding of WT podocytes on CDMs.
(I and J) Cell adhesion of WT podocytes is decreased on CDMs derived from KO cells compared to that from WT CDMs (n = 3 independent experiments and 2–3 replicates per clone and experiment were analyzed; ***$p < 0.001$, ****$p < 0.0001$; data were normalized to the mean of WT CDM).
(K and L) Enrichment of CDMs with collagen or laminin-521 ameliorates adhesion phenotypes on KO CDMs (3 replicates per clone were analyzed, normalized to the mean of WT CDM; ****$p < 0.0001$). Data are represented as mean ± SEM.

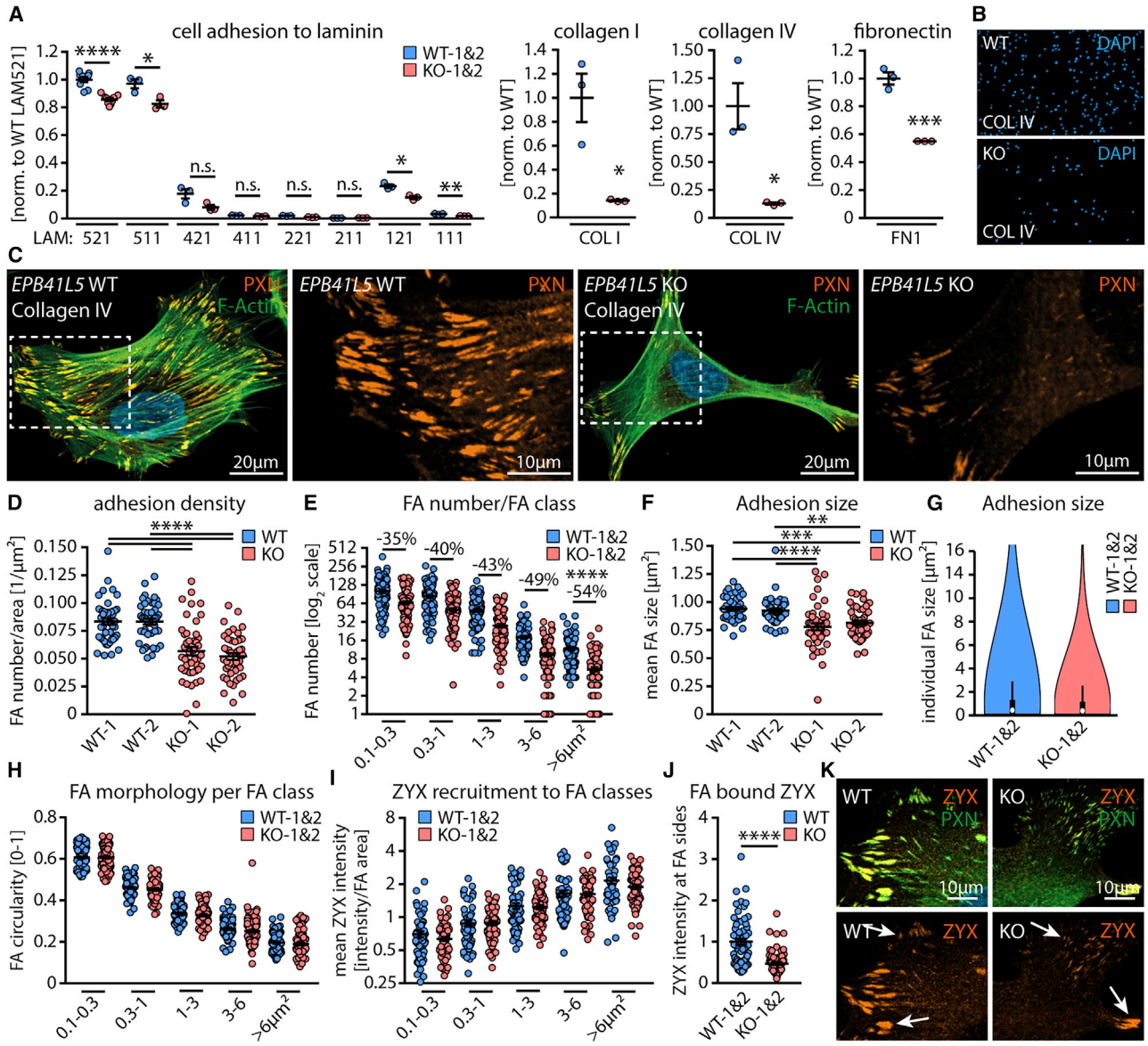

Figure 4. EPB41L5 controls IAC function

(A and B) Integrin-receptor-mediated cell adhesion of *EPB41L5* KO podocytes is specifically impaired on defined ECM ligands (LAM, laminin; 3–9 replicates per clone and ligand; *p < 0.05, **p < 0.01, ***p < 0.001, ****p < 0.0001; data were normalized to the mean of WT).

(C–G) Focal adhesion (FA) number and size are decreased in *EPB41L5* KO podocytes cultured on collagen IV substratum. Representative cells were stained for the FA marker paxillin (PXN) and F-actin (phalloidin) (boxed regions indicate zoomed-in details). Quantification of FA numbers indicates a decreased FA density (D) with a pronounced loss of matured adhesion classes in KO podocytes (E). Concomitantly mean adhesion size is reduced (F) and the relative distribution of FA size is shifted to smaller FAs in KO podocytes (G) (as shown by violin plots of 24,593 WT and 15,556 KO FAs; see also STAR Methods section for details).

(H and I) FA circularity and recruitment of the mechanosensitive FA protein ZYX are not significantly different between WT and KO cells.

(J and K) Total level of FA-bound ZYX per individual cell is decreased in *EPB41L5* KO podocytes correlating with a pronounced loss of matured FA classes (force-dependent FAs, white arrows indicate different FA classes; n = 3; dots indicate individual cells; at least 15 cells per experiment and genotype; **p < 0.01, ***p < 0.001, ****p < 0.0001). Data are represented as mean ± SEM.

with the RhoGEF ARHGEF18 (Schell et al., 2017). Therefore, we asked whether EPB41L5-dependent effects on the adhesome are primarily mediated through signaling or direct protein/complex formation. Endogenous immunoprecipitation studies indicated that EPB41L5 is capable of forming an (indirect) protein complex with PDLIM5 and ACTN4 (Figure S7), whereas other bona fide IAC components such as ZYX or VASP were not detected by this approach. These findings imply that EPB41L5 fine-tunes the IAC composition of podocytes through indirect recruitment of PDLIM5 and ACTN4 in an ARHGEF18/RhoA/

CellPress
OPEN ACCESS

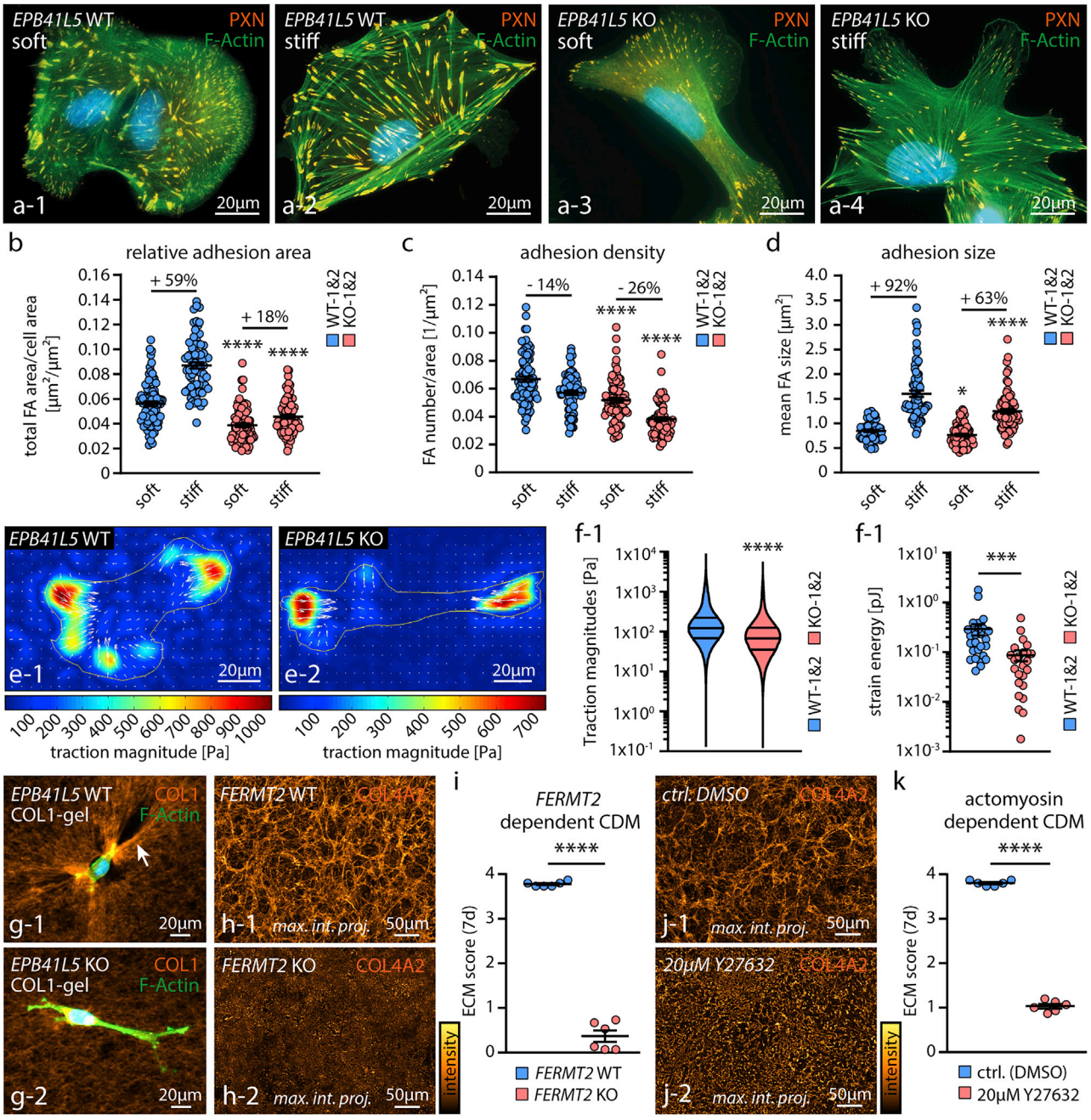

Figure 5. EPB41L5 controls podocyte matrix remodeling by force-dependent adhesion maturation

(A and B) Substrate-stiffness-dependent FA maturation is impaired in *EPB41L5* KO podocytes. Substrate-stiffness-induced increase of total adhesion area is reduced in KO podocytes, as demonstrated by quantification of FA area.

(C and D) In line with this observation, adhesion density and concomitantly adhesion size are decreased in *EPB41L5* KO podocytes depending on matrix rigidity (cells from 3 independent experiments and >20 cells per experiment, genotype, and substrate were analyzed; *$p < 0.05$, ****$p < 0.0001$).

(E and F) Traction force microscopy demonstrates decreased traction forces and strain energy of *EPB41L5* KO cells (pseudo-colored force maps, note difference in individual traction scale between WT and KO cells; 27 WT [polled WT1 and WT2] and 24 KO [polled KO1 and KO2] cells were analyzed; ***$p < 0.001$, ****$p < 0.0001$).

(G) Compaction of collagen fibers by *EPB41L5* KO podocytes is reduced on polymerized collagen I gels (white arrows indicate collagen I bundles).

(H–K) Impaired integrin-mediated mechanotransduction in podocytes by KO of *FERMT2* or inhibition of actomyosin contractility by Y27632 recapitulates ECM phenotypes, as observed in *EPB41L5* KO cells (maximum intensity projections are shown; fluorescence intensities were transformed to gold LUT; 3 independent experiments with 2 replicates per experiment and condition were analyzed; ****$p < 0.0001$). Data are represented as mean ± SEM.

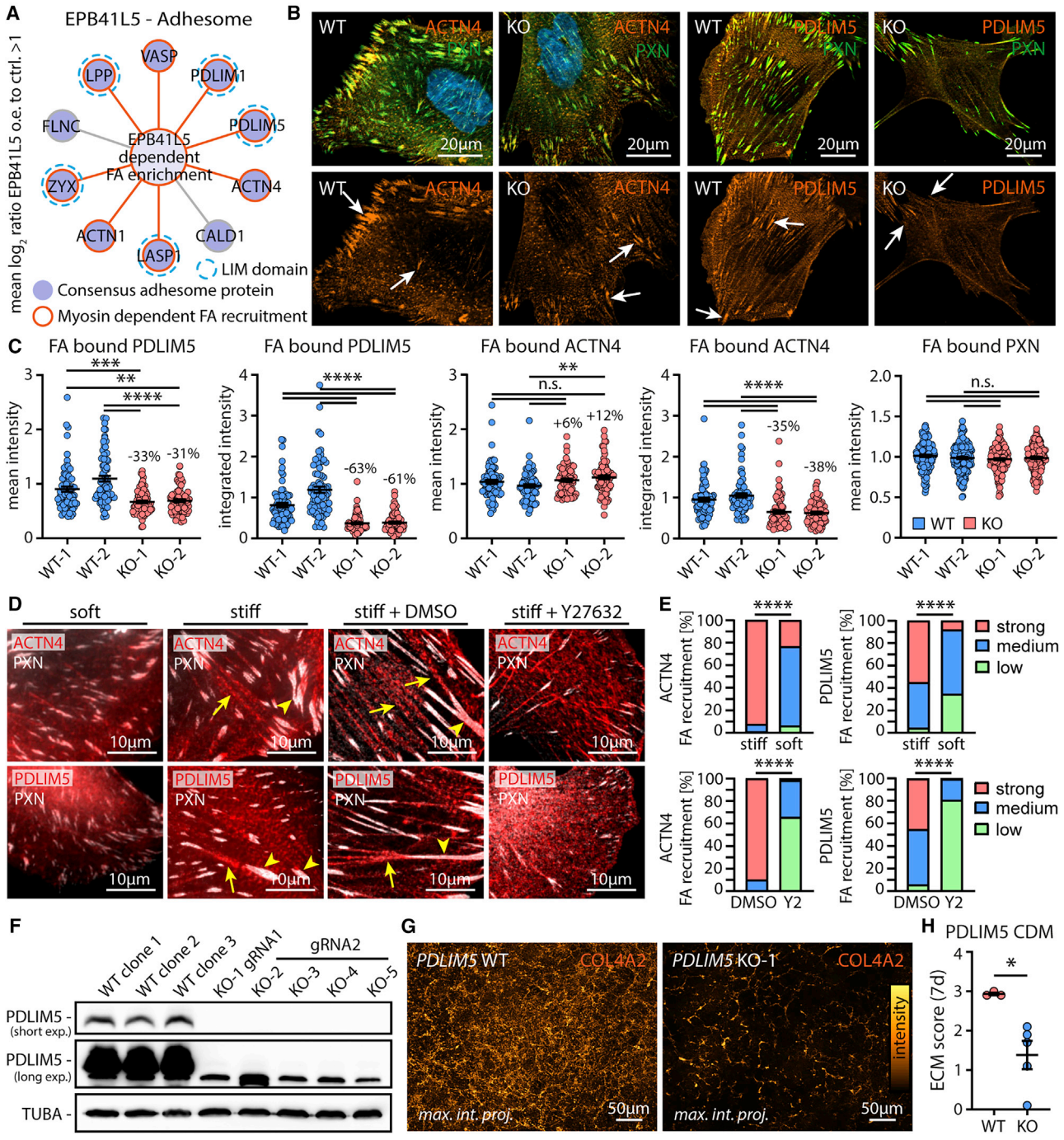

Figure 6. ACTN4 and PDLIM5 recruitment to the integrin adhesome is promoted via EPB41L5

(A) Map of SILAC-based quantitative EPB41L5-dependent integrin adhesome. Myosin-II-dependent adhesome proteins are highlighted by red circles and LIM domains by blue dotted circles.

(B) Recruitment of ACTN4 and PDLIM5 to integrin adhesion sites is impaired due to a deficiency of EPB41L5 (white arrows indicate FAs co-stained with PXN).

(C) FA recruitment of PDLIM5 and ACTN4 was analyzed by fluorescence intensity measurements of individual FAs. PXN staining was used for segmentation of FAs (scatter dots show mean and integrated intensity values for individual cells; 3 independent experiments and 20–30 cells per experiment and condition were analyzed; $^{**}p < 0.01$, $^{***}p < 0.001$, $^{****}p < 0.0001$).

(D and E) ACTN4 and PDLIM5 recruitment to integrin adhesions and the actomyosin cytoskeleton depends on substrate stiffness and actomyosin contractility (podocytes were cultured on soft [1.5-kPa gel] or stiff [glass] substrates for 24 h; 10 μM of the ROCK inhibitor Y27632 or DMSO control was applied for 1 h; yellow arrows indicate recruitment and sarcomere-like pattern of ACTN4 and PDLIM5 at actomyosin filament, and yellow arrowheads indicate recruitment to integrin adhesions; 3 independent experiments and 100 cells per experiment and condition were analyzed; $^{****}p < 0.0001$).

(legend continued on next page)

ROCK/actomyosin-dependent manner. To test the impact of this EPB41L5-dependent IAC modulation on ECM regulation, we generated *PDLIM5* KO podocytes by CRISPR-Cas9 genome editing (Figure 6F). IF analysis revealed a decreased assembly of collagen IV fibers and structural alterations characterized by overall decreased filament density due to a loss of PDLIM5, which resembled ECM phenotypes also observed in *EPB41L5* KO podocytes (Figures 6G and 6H). The pathophysiological relevance of the EPB41L5/PDLIM5/ACTN4 complex for an intact glomerular filtration barrier was further substantiated by mRNA co-expression analysis for various glomerular disease entities, demonstrating pronounced downregulation of these proteins (Figure S7; Table S2; Schell et al., 2017). In line with these findings, we evaluated localization patterns for EPB41L5 and PDLIM5 in well-established mouse models of podocyte disease (Figure 7; Figure S7). Interestingly, an increased recruitment toward regions devoid of slit diaphragms for EPB41L5 and PDLIM5 was noted (Figure 7A). These observations imply a compensatory response and role of the EPB41L5/PDLIM5/ACTN4 complex, which was initiated by IAC and cytoskeletal remodeling in podocyte disease (Figure 7B).

DISCUSSION

Despite significant progress in understanding the molecular architecture of the kidney filtration barrier (Schell et al., 2017; Lennon et al., 2014a), the contribution of the integrin adhesome remains unknown.

We observed that the loss of the podocyte-specific adhesome component EPB41L5 resulted in structural GBM abnormalities, including incomplete fusion of the endothelial and podocyte basal membrane during GBM development (Figure 1; Figure S2). The specificity of this phenotype was further validated by a pronounced defect in ECM deposition *in vitro*, excluding secondary effects such as proteinuria (Figure 1). Mechanistic insight regarding specific modes of BM synthesis *in vivo* is limited due to experimental accessibility. Therefore, most data are derived from studies using model systems such as *Caenorhabditis elegans* and *Drosophila melanogaster* (Hamill et al., 2009; Morrissey and Sherwood, 2015; Ramos-Lewis and Page-McCaw, 2019). However, it is widely accepted that collagens and laminins are secreted into the extracellular space and self-polymerize into complex networks (Hamill et al., 2009; Chew and Lennon, 2018). Moreover, maturation of the glomerular filtration barrier depends on a major shift in GBM composition, highlighting the complex process of GBM development. Recently, *in vitro* systems have mapped the global ECM profile and interplay of podocytes and glomerular endothelial cells at the proteome level, illustrating the validity and versatility of CDM models to elucidate certain aspects of GBM biology (Byron et al., 2014). By analyzing secretome and matrisome signatures of WT and *EPB41L5* KO podocytes, we detected that two core ECM proteins (collagen IV and laminin-521/-511) showed an inverse correlation between the soluble and insoluble matrix fraction (Figures 2 and 3). Although both proteins showed decreased incorporation into the insoluble ECM, high abundance was detected in the soluble fraction. These observations implied that matrix degradation processes (e.g., by MMPs) might be mediating this phenotype. Based on a set of co-culturing approaches, we demonstrated that secreted factors did not cause this phenotype (Figures 2 and 3). Instead, our observations demonstrated that the observed ECM phenotype was derived from cell-inherent effects of EPB41L5 controlling ECM assembly rather than secretory or indirect alterations (e.g., para- or autocrine mediated).

As an alternative to a secretion-dependent mode of BM assembly, one current concept proposes that ligand-matrix interactions might initially lead to immobilization of soluble ECM components and further facilitate spatially restricted polymerization as well as stabilization of the initial matrix scaffold (Hamill et al., 2009). Studies using embryonic bodies as model systems contributed to the notion that integrins are directly involved in BM assembly, thereby affecting the compositional architecture of ECM (Li et al., 2017; Aumailley et al., 2000). Remarkably, previous studies focusing on embryonic gastrulation reported that BMs were less established in *Epb41l5* null embryos than in WT control mice (Hirano et al., 2008). Studies in *C. elegans* demonstrated that integrin heterodimer composition differentially influences matrix deposition required for efficient BM assembly and shaping *in vivo* (Jayadev et al., 2019). In the context of the GBM, observations in several *in vivo* KO models targeting specific integrin subunits like *Itga3* and *Itgb1* imply that cell-adhesion receptors are involved in the process of GBM synthesis and assembly (Pozzi et al., 2008; Kreidberg et al., 1996). These findings are furthermore substantiated by the detection of structural GBM abnormalities in individuals affected by disease-causing *ITGA3* mutations (Has et al., 2012). Although these studies clearly establish a critical role for integrins in ECM/GBM assembly, underlying mechanisms and the involvement of specific adhesome components in these processes remain uncharacterized.

Based on the known function of EPB41L5 in IAC formation (Schell et al., 2017; Hirano et al., 2008), we hypothesized that EPB41L5 might affect additional integrin-receptor functions specifically related to ECM assembly. Indeed, a detailed characterization of EPB41L5 KO podocytes revealed that the loss of EPB41L5 not only resulted in a diminished integrin affinity toward ECM ligands but also caused decreased integrin adhesion maturation and traction force (Figures 4 and 5). IACs directly connect the surrounding ECM and the intracellular actin cytoskeleton, allowing bidirectional force transmission. In general, this interplay results in progressive integrin adhesion reinforcement, characterized by further recruitment of proteins to the IAC and adhesion site formation (Kechagia et al., 2019). Integrin affinity and adhesion reinforcement rely on Talin-1, Kindlin-2 (*FERMT2*), and mechanical forces to promote the extended-open conformation of beta-integrins (Sun

(F) Western blot analysis of *PDLIM5* CRISPR-Cas9 KO and WT clones confirms loss of PDLIM5 in respective KO podocytes.
(G) COL4A2 immunofluorescence analysis of decellularized ECM demonstrates decreased levels of collagen IV network density in *PDLIM5* KO matrices (fluorescence intensities were transformed to gold LUT, as indicated by intensity charts).
(H) Semiquantitative ECM scoring of *PDLIM5* CDMs synthesized over 7 days (scatter dots indicate individual WT and KO clones; *$p < 0.05$). Data are represented as mean ± SEM.

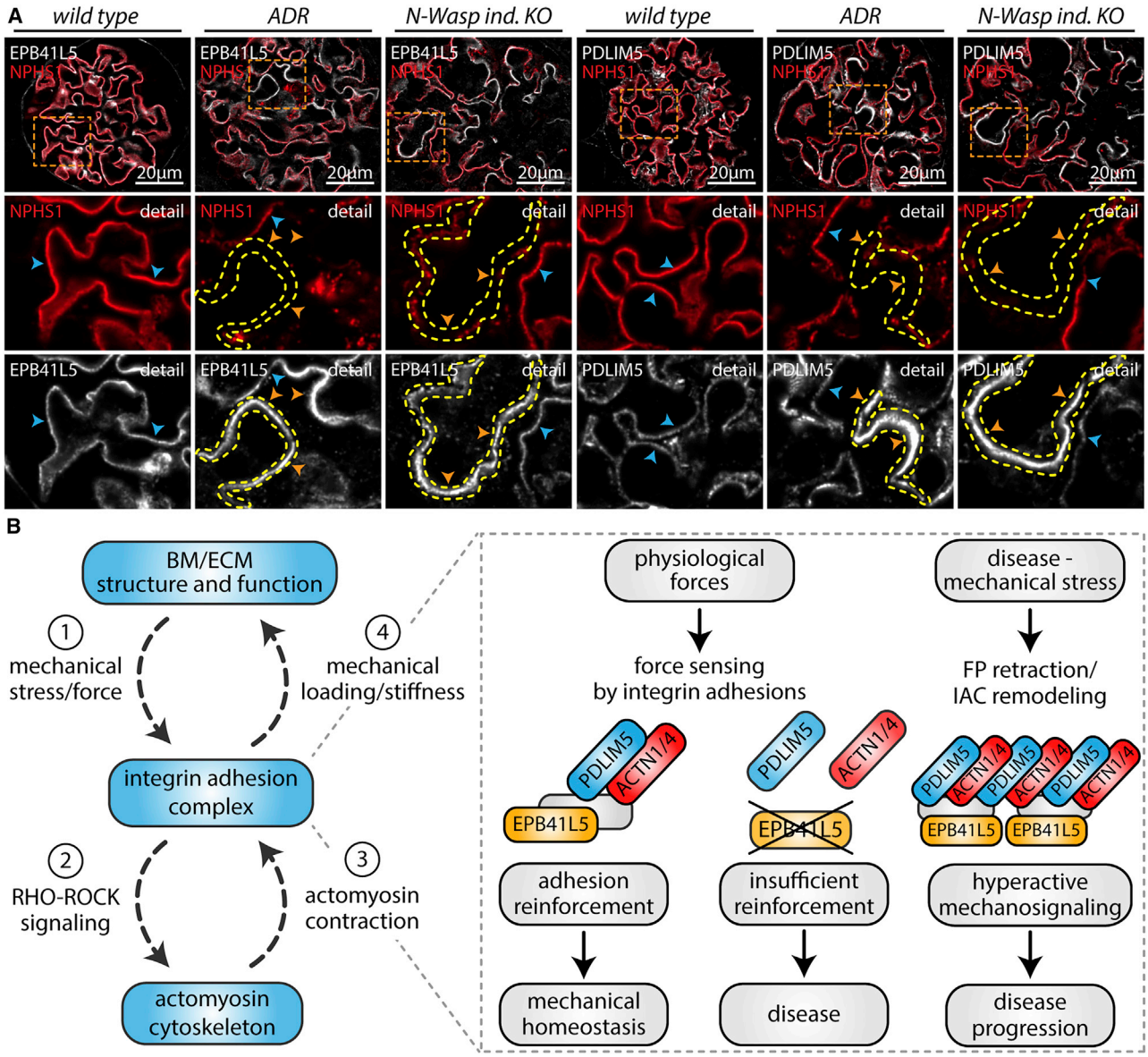

Figure 7. EPB41L5 and PDLIM5 localization is disturbed in podocyte disease

(A) EPB41L5 and PDLIM5 localization is disturbed in murine models of podocyte disease, as demonstrated by immunofluorescence analysis. EPB41L5 and PDLIM5 recruitment is highly increased at regions with FP retraction, as demonstrated by reduced expression of the slit diaphragm marker NPHS1 (orange arrowheads and yellow dashed lines). Regions with unaffected NPHS1 localization showed no increased or slightly decreased EPB41L5 and PDLIM5 recruitment (blue arrowheads). Glomeruli of mice with adriamycin (ADR)-induced glomerulopathy as well as a podocyte-specific genetic focal segmental glomerulosclerosis (FSGS) model (*N-WASP* podocyte specific KO) were analyzed (boxed regions indicate zoomed-in details). Representative glomeruli at the early phase of podocyte disease were analyzed as indicated by moderate alterations of NPHS1 expression and localization in these glomeruli.

(B) Graphical summary of proposed EPB41L5-mediated functions in homeostasis of podocyte GBM and IAC properties.

et al., 2019). Remarkably, a recent study demonstrated that integrin binding by these adapters and cytoskeletal force are sufficient to enable integrin activation by forces in the low pN range (Li and Springer, 2017; Sun et al., 2019). Adhesome composition-dependent regulation of ultrasensitive integrin activation by physiological forces might represent an essential feature of IACs at podocyte foot processes and explain the profound phenotype caused by the podocyte-specific deletion of *Itgb1*, *Tln1*, *Fermt2*, and *Epb41l5* (Kreidberg et al., 1996; Tian et al., 2014; Yasuda-Yamahara et al., 2018a). We observed similar phenotypes of disturbed ECM assembly and deposition caused by the loss of EPB41L5, when testing this mechanism in the context of ECM assembly, by using *FERMT2* KO podocytes and actomyosin inhibition (Figure 5). These findings extend the concept of IACs as sole ligation spots for ECM assembly and integrate force signaling as an additional aspect of podocyte-mediated ECM organization and shaping.

Proteomic analysis of EPB41L5-enriched IACs indicated that EPB41L5 facilitates the recruitment of myosin-II-dependent adhesion components such as ACTN4 and PDLIM5, thereby modulating the repertoire of individual IACs (Figure 6). PDLIM5 belongs to the enigma protein subfamily and contains an N-terminal PDZ domain as well as C-terminal LIM-domains, which enable linkage to α-Actinin and other proteins (Verdonschot et al., 2020). More recently, PDLIM5 and α-Actinin have been implicated in force transmission and mechano-transduction signaling at IACs (Elbediwy et al., 2018; Ajeian et al., 2016; Meacci et al., 2016; Feng et al., 2018; Roca-Cusachs et al., 2013). In line with these reports, PDLIM5 recruitment to IACs was EPB41L5- and mechano-dependent in podocytes (Figure 6). Moreover, *PDLIM5* KO podocytes resembled ECM phenotypes of *EPB41L5* KO cells (Figure 6). Although there is the notion that podocytes as specialized pericyte-like cells are exposed to continuous physical forces, there is only limited knowledge about how podocytes integrate these signals (Endlich et al., 2017). Based on our observations, we propose a model in which EPB41L5 is modulating the repertoire of podocyte IACs, which finally translates into IAC reinforcement and ECM remodeling (Figure 7B), i.e., EPB41L5 stimulates RhoA/actomyosin signaling at IACs by directly interacting with ARHGEF18 (Schell et al., 2017). The impaired integration of collagens and laminins in CDMs from *EPB41L5* KO cells can be at least partially attributed to reduced levels of actomyosin contractility and IAC traction (Figure 5). In fact, there is ample evidence for actomyosin-mediated contractile forces in fibrillogenesis of fibronectin. Here, physical stretching of fibronectin leads to a release of cryptic binding sites within the fibronectin molecule, which in turn initiate and facilitate further fibronectin assembly (Lu et al., 2020; Danen et al., 2002). Moreover, the involvement of RhoA in maintaining the BM during embryonic gastrulation has been shown before, highlighting the essential role of epistatic force balance in cell-matrix interactions (Nakaya et al., 2008). Our observations have major implications for glomerular diseases, for which a decreased abundance of adhesion receptors not only results in podocyte detachment but also affects ECM integrity and stability. Actin cytoskeleton reorganization, RhoA/actomyosin activation, and podocyte detachment are frequently observed in glomerular disease (Perico et al., 2016; Suleiman et al., 2017). Moreover, very recently, an elegant study introduced podocyte compressive forces toward the GBM as major determinants to counteract filtration pressure and maintain the filtration barrier (Butt et al., 2020). Thus, maladaptation of the adhesome might initiate a self-perpetuating cascade, leading to GBM remodeling and progressive impairment of the filtration barrier integrity in glomerular disease.

STAR★METHODS

Detailed methods are provided in the online version of this paper and include the following:

SUPPLEMENTAL INFORMATION

Supplemental Information can be found online at https://doi.org/10.1016/j.celrep.2021.108883.

ACKNOWLEDGMENTS

We would like to thank Charlotte Meyer and Severine Kayser for expert technical assistance. In addition, we would like to express our gratitude to all members of our laboratories and to the Core Facility Electron Microscopy, Department of Nephrology, Faculty of Medicine, University of Freiburg, Germany, for helpful discussions and support. The work contains parts of the thesis of J.I.M. and the thesis of M.R. This study was supported by the German Research Foundation (DFG - Deutsche Forschungsgemeinschaft - CRC1192, HU 1016/8-2, HU 1016/11-1, and HU 1016/ 12-1 to T.B.H.; SCHE 2092/1-2 and SCHE 2092/3-1 to C.S.); the Else Kröner-Fresenius-Stiftung (2016_Kolleg.03 to M.R.) and Else Kröner-Fresenius-Stiftung Matriglom (EKFS A_09 to C.S.); the Berta-Ottenstein Programme, Faculty of Medicine, University of Freiburg (to C.S.); and by the National Institutes of Health (R01DK058366 and R01DK078314 to J.H.M.). The article processing charge was funded by the Baden-Wuerttemberg Ministry of Science, Research and Art and the University of Freiburg in the funding programme Open Access Publishing.

AUTHOR CONTRIBUTIONS

J.I.M., M.R., M.H., O.S. B.S., J.D., and C.S. conceived and analyzed experiments. M.R., G.W., M.W., T.B.H., and C.S. supervised the study. J.I.M., M.R., M.H., A.S., and C.S. performed experiments. J.H.M. provided critical reagents. J.I.M., M.R., and C.S. wrote the manuscript with input and discussion from all authors.

DECLARATION OF INTERESTS

All authors declare no competing interests.

Received: May 26, 2020
Revised: December 21, 2020
Accepted: February 25, 2021
Published: March 23, 2021

REFERENCES

Ajeian, J.N., Horton, E.R., Astudillo, P., Byron, A., Askari, J.A., Millon-Frémillon, A., Knight, D., Kimber, S.J., Humphries, M.J., and Humphries, J.D. (2016). Proteomic analysis of integrin-associated complexes from mesenchymal stem cells. Proteomics Clin. Appl. *10*, 51–57.

Aumailley, M., Pesch, M., Tunggal, L., Gaill, F., and Fässler, R. (2000). Altered synthesis of laminin 1 and absence of basement membrane component deposition in (beta)1 integrin-deficient embryoid bodies. J. Cell Sci. *113*, 259–268.

Barger, C.J., Branick, C., Chee, L., and Karpf, A.R. (2019). Pan-Cancer Analyses Reveal Genomic Features of FOXM1 Overexpression in Cancer. Cancers (Basel) *11*, 251.

Biniossek, M.L., Niemer, M., Maksimchuk, K., Mayer, B., Fuchs, J., Huesgen, P.F., McCafferty, D.G., Turk, B., Fritz, G., Mayer, J., et al. (2016). Identification of Protease Specificity by Combining Proteome-Derived Peptide Libraries and Quantitative Proteomics. Mol. Cell. Proteomics *15*, 2515–2524.

Boerries, M., Grahammer, F., Eiselein, S., Buck, M., Meyer, C., Goedel, M., Bechtel, W., Zschiedrich, S., Pfeifer, D., Laloë, D., et al. (2013). Molecular fingerprinting of the podocyte reveals novel gene and protein regulatory networks. Kidney Int. *83*, 1052–1064.

Brigstock, D.R. (2002). Regulation of angiogenesis and endothelial cell function by connective tissue growth factor (CTGF) and cysteine-rich 61 (CYR61). Angiogenesis *5*, 153–165.

Butt, L., Unnersjö-Jess, D., Höhne, M., Edwards, A., Binz-Lotter, J., Reilly, D., Hahnfeldt, R., Ziegler, V., Fremter, K., Rinschen, M.M., et al. (2020). A molecular mechanism explaining albuminuria in kidney disease. Nat. Metab. *2*, 461–474.

Byron, A., Randles, M.J., Humphries, J.D., Mironov, A., Hamidi, H., Harris, S., Mathieson, P.W., Saleem, M.A., Satchell, S.C., Zent, R., et al. (2014). Glomerular cell cross-talk influences composition and assembly of extracellular matrix. J. Am. Soc. Nephrol. *25*, 953–966.

Chew, C., and Lennon, R. (2018). Basement Membrane Defects in Genetic Kidney Diseases. Front Pediatr. *6*, 11.

Danen, E.H., Sonneveld, P., Brakebusch, C., Fassler, R., and Sonnenberg, A. (2002). The fibronectin-binding integrins alpha5beta1 and alphavbeta3 differentially modulate RhoA-GTP loading, organization of cell matrix adhesions, and fibronectin fibrillogenesis. J. Cell Biol. *159*, 1071–1086.

Elbediwy, A., Vanyai, H., Diaz-de-la-Loza, M.D., Frith, D., Snijders, A.P., and Thompson, B.J. (2018). Enigma proteins regulate YAP mechanotransduction. J. Cell Sci. *131*, jcs221788.

Endlich, K., Kliewe, F., and Endlich, N. (2017). Stressed podocytes-mechanical forces, sensors, signaling and response. Pflugers Arch. *469*, 937–949.

Feng, D., Notbohm, J., Benjamin, A., He, S., Wang, M., Ang, L.H., Bantawa, M., Bouzid, M., Del Gado, E., Krishnan, R., and Pollak, M.R. (2018). Disease-causing mutation in α-actinin-4 promotes podocyte detachment through maladaptation to periodic stretch. Proc. Natl. Acad. Sci. USA *115*, 1517–1522.

Funk, S.D., Lin, M.H., and Miner, J.H. (2018). Alport syndrome and Pierson syndrome: Diseases of the glomerular basement membrane. Matrix Biol. *71–72*, 250–261.

Grahammer, F., Schell, C., and Huber, T.B. (2013). The podocyte slit diaphragm–from a thin grey line to a complex signalling hub. Nat. Rev. Nephrol. *9*, 587–598.

Hamill, K.J., Kligys, K., Hopkinson, S.B., and Jones, J.C. (2009). Laminin deposition in the extracellular matrix: a complex picture emerges. J. Cell Sci. *122*, 4409–4417.

Has, C., Spartà, G., Kiritsi, D., Weibel, L., Moeller, A., Vega-Warner, V., Waters, A., He, Y., Anikster, Y., Esser, P., et al. (2012). Integrin α3 mutations with kidney, lung, and skin disease. N. Engl. J. Med. *366*, 1508–1514.

Hirano, M., Hashimoto, S., Yonemura, S., Sabe, H., and Aizawa, S. (2008). EPB41L5 functions to post-transcriptionally regulate cadherin and integrin during epithelial-mesenchymal transition. J. Cell Biol. *182*, 1217–1230.

Hohenester, E., and Yurchenco, P.D. (2013). Laminins in basement membrane assembly. Cell Adhes. Migr. *7*, 56–63.

Humphrey, J.D., Dufresne, E.R., and Schwartz, M.A. (2014). Mechanotransduction and extracellular matrix homeostasis. Nat. Rev. Mol. Cell Biol. *15*, 802–812.

Humphries, M.J. (2009). Cell adhesion assays. Methods Mol. Biol. *522*, 203–210.

Hynes, R.O., and Naba, A. (2012). Overview of the matrisome–an inventory of extracellular matrix constituents and functions. Cold Spring Harb. Perspect. Biol. *4*, a004903.

Jayadev, R., Chi, Q., Keeley, D.P., Hastie, E.L., Kelley, L.C., and Sherwood, D.R. (2019). α-Integrins dictate distinct modes of type IV collagen recruitment to basement membranes. J. Cell Biol. *218*, 3098–3116.

Kaukonen, R., Jacquemet, G., Hamidi, H., and Ivaska, J. (2017). Cell-derived matrices for studying cell proliferation and directional migration in a complex 3D microenvironment. Nat. Protoc. *12*, 2376–2390.

Kechagia, J.Z., Ivaska, J., and Roca-Cusachs, P. (2019). Integrins as biomechanical sensors of the microenvironment. Nat. Rev. Mol. Cell Biol. *20*, 457–473.

Kreidberg, J.A., Donovan, M.J., Goldstein, S.L., Rennke, H., Shepherd, K., Jones, R.C., and Jaenisch, R. (1996). Alpha 3 beta 1 integrin has a crucial role in kidney and lung organogenesis. Development *122*, 3537–3547.

Kuo, J.C., Han, X., Hsiao, C.T., Yates, J.R., III, and Waterman, C.M. (2011). Analysis of the myosin-II-responsive focal adhesion proteome reveals a role for β-Pix in negative regulation of focal adhesion maturation. Nat. Cell Biol. *13*, 383–393.

Labun, K., Montague, T.G., Krause, M., Torres Cleuren, Y.N., Tjeldnes, H., and Valen, E. (2019). CHOPCHOP v3: expanding the CRISPR web toolbox beyond genome editing. Nucleic Acids Res. *47*, W171–W174.

Lennon, R., Byron, A., Humphries, J.D., Randles, M.J., Carisey, A., Murphy, S., Knight, D., Brenchley, P.E., Zent, R., and Humphries, M.J. (2014a). Global analysis reveals the complexity of the human glomerular extracellular matrix. J. Am. Soc. Nephrol. *25*, 939–951.

Lennon, R., Randles, M.J., and Humphries, M.J. (2014b). The importance of podocyte adhesion for a healthy glomerulus. Front. Endocrinol. (Lausanne) *5*, 160.

Li, J., and Springer, T.A. (2017). Integrin extension enables ultrasensitive regulation by cytoskeletal force. Proc. Natl. Acad. Sci. USA *114*, 4685–4690.

Li, S., Qi, Y., McKee, K., Liu, J., Hsu, J., and Yurchenco, P.D. (2017). Integrin and dystroglycan compensate each other to mediate laminin-dependent basement membrane assembly and epiblast polarization. Matrix Biol. *57–58*, 272–284.

Lu, J., Doyle, A.D., Shinsato, Y., Wang, S., Bodendorfer, M.A., Zheng, M., and Yamada, K.M. (2020). Basement Membrane Regulates Fibronectin Organization Using Sliding Focal Adhesions Driven by a Contractile Winch. Dev. Cell *52*, 631–646.e4.

Meacci, G., Wolfenson, H., Liu, S., Stachowiak, M.R., Iskratsch, T., Mathur, A., Ghassemi, S., Gauthier, N., Tabdanov, E., Lohner, J., et al. (2016). α-Actinin links extracellular matrix rigidity-sensing contractile units with periodic cell-edge retractions. Mol. Biol. Cell *27*, 3471–3479.

Miner, J.H., and Sanes, J.R. (1994). Collagen IV alpha 3, alpha 4, and alpha 5 chains in rodent basal laminae: sequence, distribution, association with laminins, and developmental switches. J. Cell Biol. *127*, 879–891.

Moeller, M.J., Sanden, S.K., Soofi, A., Wiggins, R.C., and Holzman, L.B. (2003). Podocyte-specific expression of cre recombinase in transgenic mice. Genesis *35*, 39–42.

Morrissey, M.A., and Sherwood, D.R. (2015). An active role for basement membrane assembly and modification in tissue sculpting. J. Cell Sci. *128*, 1661–1668.

Mouw, J.K., Ou, G., and Weaver, V.M. (2014). Extracellular matrix assembly: a multiscale deconstruction. Nat. Rev. Mol. Cell Biol. *15*, 771–785.

Naba, A., Clauser, K.R., Ding, H., Whittaker, C.A., Carr, S.A., and Hynes, R.O. (2016). The extracellular matrix: Tools and insights for the "omics" era. Matrix Biol. *49*, 10–24.

Nakaya, Y., Sukowati, E.W., Wu, Y., and Sheng, G. (2008). RhoA and microtubule dynamics control cell-basement membrane interaction in EMT during gastrulation. Nat. Cell Biol. *10*, 765–775.

Nicolaou, N., Margadant, C., Kevelam, S.H., Lilien, M.R., Oosterveld, M.J., Kreft, M., van Eerde, A.M., Pfundt, R., Terhal, P.A., van der Zwaag, B., et al. (2012). Gain of glycosylation in integrin α3 causes lung disease and nephrotic syndrome. J. Clin. Invest. *122*, 4375–4387.

Perico, L., Conti, S., Benigni, A., and Remuzzi, G. (2016). Podocyte-actin dynamics in health and disease. Nat. Rev. Nephrol. *12*, 692–710.

Plotnikov, S.V., Sabass, B., Schwarz, U.S., and Waterman, C.M. (2014). High-resolution traction force microscopy. Methods Cell Biol. *123*, 367–394.

Pozzi, A., Jarad, G., Moeckel, G.W., Coffa, S., Zhang, X., Gewin, L., Eremina, V., Hudson, B.G., Borza, D.B., Harris, R.C., et al. (2008). Beta1 integrin expression by podocytes is required to maintain glomerular structural integrity. Dev. Biol. *316*, 288–301.

Ramos-Lewis, W., and Page-McCaw, A. (2019). Basement membrane mechanics shape development: Lessons from the fly. Matrix Biol. *75–76*, 72–81.

Randles, M.J., Lausecker, F., Humphries, J.D., Byron, A., Clark, S.J., Miner, J.H., Zent, R., Humphries, M.J., and Lennon, R. (2020). Basement membrane ligands initiate distinct signalling networks to direct cell shape. Matrix Biol. *90*, 61–78.

Rinschen, M.M., Gödel, M., Grahammer, F., Zschiedrich, S., Helmstädter, M., Kretz, O., Zarei, M., Braun, D.A., Dittrich, S., Pahmeyer, C., et al. (2018). A Multi-layered Quantitative In Vivo Expression Atlas of the Podocyte Unravels Kidney Disease Candidate Genes. Cell Rep. *23*, 2495–2508.

Roca-Cusachs, P., del Rio, A., Puklin-Faucher, E., Gauthier, N.C., Biais, N., and Sheetz, M.P. (2013). Integrin-dependent force transmission to the extracellular matrix by α-actinin triggers adhesion maturation. Proc. Natl. Acad. Sci. USA *110*, E1361–E1370.

Rogg, M., Yasuda-Yamahara, M., Abed, A., Dinse, P., Helmstädter, M., Conzelmann, A.C., Frimmel, J., Sellung, D., Biniossek, M.L., Kretz, O., et al. (2017). The WD40-domain containing protein CORO2B is specifically enriched in glomerular podocytes and regulates the ventral actin cytoskeleton. Sci. Rep. *7*, 15910.

Rogg, M., Maier, J.I., Dotzauer, R., Artelt, N., Kretz, O., Helmstädter, M., Abed, A., Sammarco, A., Sigle, A., Sellung, D., et al. (2021). SRGAP1 Controls Small Rho GTPases To Regulate Podocyte Foot Process Maintenance. J. Am. Soc. Nephrol. *32*, 563–579.

Saleem, M.A., O'Hare, M.J., Reiser, J., Coward, R.J., Inward, C.D., Farren, T., Xing, C.Y., Ni, L., Mathieson, P.W., and Mundel, P. (2002). A conditionally immortalized human podocyte cell line demonstrating nephrin and podocin expression. J. Am. Soc. Nephrol. *13*, 630–638.

Sanjana, N.E., Shalem, O., and Zhang, F. (2014). Improved vectors and genome-wide libraries for CRISPR screening. Nat. Methods *11*, 783–784.

Sasaki, T., Mann, K., Miner, J.H., Miosge, N., and Timpl, R. (2002). Domain IV of mouse laminin beta1 and beta2 chains. Eur. J. Biochem. *269*, 431–442.

Sawai, K., Mukoyama, M., Mori, K., Kasahara, M., Koshikawa, M., Yokoi, H., Yoshioka, T., Ogawa, Y., Sugawara, A., Nishiyama, H., et al. (2007). Expression of CCN1 (CYR61) in developing, normal, and diseased human kidney. Am. J. Physiol. Renal Physiol. *293*, F1363–F1372.

Schell, C., Baumhakl, L., Salou, S., Conzelmann, A.C., Meyer, C., Helmstädter, M., Wrede, C., Grahammer, F., Eimer, S., Kerjaschki, D., et al. (2013). N-wasp is required for stabilization of podocyte foot processes. J. Am. Soc. Nephrol. *24*, 713–721.

Schell, C., Kretz, O., Bregenzer, A., Rogg, M., Helmstädter, M., Lisewski, U., Gotthardt, M., Tharaux, P.L., Huber, T.B., and Grahammer, F. (2015). Podocyte-Specific Deletion of Murine CXADR Does Not Impair Podocyte Development, Function or Stress Response. PLoS One *10*, e0129424.

Schell, C., Rogg, M., Suhm, M., Helmstädter, M., Sellung, D., Yasuda-Yamahara, M., Kretz, O., Küttner, V., Suleiman, H., Kollipara, L., et al. (2017). The FERM protein EPB41L5 regulates actomyosin contractility and focal adhesion formation to maintain the kidney filtration barrier. Proc. Natl. Acad. Sci. USA *114*, E4621–E4630.

Schell, C., Sabass, B., Helmstaedter, M., Geist, F., Abed, A., Yasuda-Yamahara, M., Sigle, A., Maier, J.I., Grahammer, F., Siegerist, F., et al. (2018). ARP3 Controls the Podocyte Architecture at the Kidney Filtration Barrier. Dev. Cell *47*, 741–757.e8.

Schiller, H.B., Friedel, C.C., Boulegue, C., and Fässler, R. (2011). Quantitative proteomics of the integrin adhesome show a myosin II-dependent recruitment of LIM domain proteins. EMBO Rep. *12*, 259–266.

Suh, J.H., and Miner, J.H. (2013). The glomerular basement membrane as a barrier to albumin. Nat. Rev. Nephrol. *9*, 470–477.

Suleiman, H., Zhang, L., Roth, R., Heuser, J.E., Miner, J.H., Shaw, A.S., and Dani, A. (2013). Nanoscale protein architecture of the kidney glomerular basement membrane. eLife *2*, e01149.

Suleiman, H.Y., Roth, R., Jain, S., Heuser, J.E., Shaw, A.S., and Miner, J.H. (2017). Injury-induced actin cytoskeleton reorganization in podocytes revealed by super-resolution microscopy. JCI Insight *2*, e94137.

Sun, Z., Costell, M., and Fässler, R. (2019). Integrin activation by talin, kindlin and mechanical forces. Nat. Cell Biol. *21*, 25–31.

Tian, X., Kim, J.J., Monkley, S.M., Gotoh, N., Nandez, R., Soda, K., Inoue, K., Balkin, D.M., Hassan, H., Son, S.H., et al. (2014). Podocyte-associated talin1 is critical for glomerular filtration barrier maintenance. J. Clin. Invest. *124*, 1098–1113.

Toda, N., Mukoyama, M., Yanagita, M., and Yokoi, H. (2018). CTGF in kidney fibrosis and glomerulonephritis. Inflamm. Regen. *38*, 14.

Verdonschot, J.A.J., Robinson, E.L., James, K.N., Mohamed, M.W., Claes, G.R.F., Casas, K., Vanhoutte, E.K., Hazebroek, M.R., Kringlen, G., Pasierb, M.M., et al. (2020). Mutations in PDLIM5 are rare in dilated cardiomyopathy but are emerging as potential disease modifiers. Mol. Genet. Genomic Med. *8*, e1049.

Winograd-Katz, S.E., Fässler, R., Geiger, B., and Legate, K.R. (2014). The integrin adhesome: from genes and proteins to human disease. Nat. Rev. Mol. Cell Biol. *15*, 273–288.

Yasuda-Yamahara, M., Rogg, M., Frimmel, J., Trachte, P., Helmstaedter, M., Schroder, P., Schiffer, M., Schell, C., and Huber, T.B. (2018a). FERMT2 links cortical actin structures, plasma membrane tension and focal adhesion function to stabilize podocyte morphology. Matrix Biol. *68–69*, 263–279.

Yasuda-Yamahara, M., Rogg, M., Yamahara, K., Maier, J.I., Huber, T.B., and Schell, C. (2018b). AIF1L regulates actomyosin contractility and filopodial extensions in human podocytes. PLoS One *13*, e0200487.

Zhang, J., Wang, Y., Gurung, P., Wang, T., Li, L., Zhang, R., Li, H., Guo, R., Han, Q., Zhang, J., et al. (2018). The relationship between the thickness of glomerular basement membrane and renal outcomes in patients with diabetic nephropathy. Acta Diabetol. *55*, 669–679.

STAR★METHODS

KEY RESOURCES TABLE

REAGENT or RESOURCE	SOURCE	IDENTIFIER
Antibodies		
ACTN4	Abcam	Cat#ab108198; RRID:AB_10858236
ARHGEF18	Atlas Antibodies	Cat#HPA042689; RRID:AB_10794385
COL1	Novus Biologicals	Cat#NB600-408; RRID:AB_343276
COL4	Abcam	Cat#ab6586; RRID:AB_305584
COL4A2	Merck	Cat#MAB1910; RRID:AB_2082643
COL4A4	Miner and Sanes, 1994	N/A
CTTN	Cell Signaling	Cat#3503S; RRID:AB_2115160
EPB41L5	Atlas Antibodies	Cat#HPA037564; RRID:AB_2675547
EPB41L5	gen. gift R. Roepman, see Schell et al., 2017	N/A
EPB41L5	Atlas Antibodies	Cat#HPA037563; RRID:AB_2675546
FLAG M2	Merck	Cat#F3165; RRID:AB_259529
GAPDH	Abcam	Cat#ab8245; RRID:AB_2107448
LAMA5	Atlas Antibodies	Cat#AMAb91124; RRID:AB_2665809
LAMB1	Atlas Antibodies	Cat#HPA004056; RRID:AB_1079226
LAMB1	Sasaki et al., 2002	N/A
LAMB2	Atlas Antibodies	Cat#AMAB91097; RRID:AB_2665799
LAMC1	Atlas Antibodies	Cat#HPA001909; RRID:AB_1079230
NPHS1	PROGEN	Cat#GP-N2; RRID:AB_1542487
pan-ACTN (ACTN1)	Santa Cruz	Cat#sc-166524; RRID:AB_2257995
PDLIM5	Atlas Antibodies	Cat#HPA016740; RRID:AB_1855153
p-MLC	Cell Signaling	Cat#3671; RRID:AB_330248
p-MLC	Cell Signaling	Cat#3674; RRID:AB_2147464
PXN	BD Biosciences	Cat#610051; RRID:AB_397463
TLN1	Merck	Cat#T3287; RRID:AB_477572
TUBA	Merck	Cat#T9026; RRID:AB_477593
VASP	Cell Signaling	Cat#3132; RRID:AB_2213393
WT1	Abcam	Cat#ab15249; RRID:AB_301790
YAP/TAZ	Cell Signaling	Cat#8418; RRID:AB_10950494
ZYX	Atlas Antibodies	Cat#HPA004835; RRID:AB_1080771
FLAG M2 Affinity Agarose Gel	Sigma-Aldrich	Cat#A2220; RRID:AB_10063035
Alexa Fluor Phalloidin 488	Thermo Fisher Scientific	Cat#A-12379
Alexa Fluor Phalloidin 546	Thermo Fisher Scientific	Cat#A-22283; RRID:AB_2632953
Alexa Fluor 555, donkey anti-rabbit IgG	Thermo Fisher Scientific	Cat#A-31572; RRID:AB_162543
Alexa Fluor 488, goat anti-guinea pig IgG	Thermo Fisher Scientific	Cat#A-11073; RRID:AB_2534117
Alexa Fluor 555, goat anti-mouse IgG1	Thermo Fisher Scientific	Cat#A-21127; RRID:AB_2535769
Alexa Fluor 488, goat anti-mouse IgG1	Thermo Fisher Scientific	Cat#A-21121; RRID:AB_2535764
Goat anti-rabbit IgG, HRP-linked Antibody	Cell Signaling	Cat#7074; RRID:AB_2099233
Goat anti-mouse Immunglobulins/HRP	Agilent, Dako	Cat#P0447; RRID:AB_2617137
Alexa Fluor 647, goat anti-guinea pig IgG	Thermo Fisher Scientific	Cat#A-21450; RRID:AB_2735091
DAPI	Thermo Fisher Scientific	Cat#D21490

(*Continued on next page*)

Continued

REAGENT or RESOURCE	SOURCE	IDENTIFIER
Biological samples		
Mouse tissue *Epb41l5*$^{fl/fl}$*hNPHS2Cre*	Schell et al., 2017	N/A
Mouse tissue *Adriamycin nephropathy*	Schell et al., 2015	N/A
Mouse tissue N-WASP inducible	Schell et al., 2013	N/A
Chemicals, peptides, and recombinant proteins		
(3-Aminopropyl)trimethoxysilan	Sigma-Aldrich	Cat#281778
μ-Dish 35 mm, high ESS Variety Pack	Ibidi	Cat#81199
μ-Dish 35 mm, high Grid-50 Glass Bottom	Ibidi	Cat#81148
μ-Slide 2 Well Co-Culture	Ibidi	Cat#81806
μ-Slide 8 Well, Collagen IV	Ibidi	Cat#80822
2% Bis Solution; 2% bis-acrylamide solution	BioRad	Cat#1610142
40% Acrylamide Solution	BioRad	Cat#1610140
Advanced TC, cell culture dish, 145/20 MM	Greiner BIO-ONE	Cat#639960
Advanced TC, cell culture dish, 35/10 MM	Greiner BIO-ONE	Cat#627960
Biolaminin 111 LN	BioLamina	Cat#LN111
Biolaminin 121 LN	BioLamina	Cat#LN121
Biolaminin 211 LN	BioLamina	Cat#LN211
Biolaminin 221 LN	BioLamina	Cat#LN221
Biolaminin 411 LN	BioLamina	Cat#LN411
Biolaminin 421 LN	BioLamina	Cat#LN421
Biolaminin 511 LN	BioLamina	Cat#LN511
Biolaminin 521 LN	BioLamina	Cat#LN521
Bovine Type I Collagen Solution, PureCol	AdvancedBioMatrix	Cat#5005
Collagen IV from human placenta	Sigma-Aldrich	Cat#C5533
Collagenase, Type 2	Worthington Biochemical	Cat#LS004176
DNase I	AppliChem	Cat#A3778
Fibronectin	Corning	Cat#354008
FluoSpheres Carboxylate-Modified Microspheres, 0.04 μm, red-orange fluorescent (565/580)	Thermo Fisher Scientific	Cat#F8794
Gelatin	Sigma-Aldrich	Cat#G1890
Glass Bottom Dish 35 mm	Ibidi	Cat#81218
L-Ascorbic acid	Sigma-Aldrich	Cat#A92902
Marimastat	Selleckchem	Cat#S7156
Non-Essential Amino Acids	Thermo Fisher Scientific	Cat#11140
Pierce Protein Concentrator PES, 10K MWCO	Thermo Fisher Scientific	Cat#88528
Protease from Streptomyces griseus	Sigma-Aldrich	Cat#P6911
Sulfo SANPAH Crosslinker	Thermo Fisher Scientific	Cat#22589
Y-27632	Selleckchem	Cat#S1049
Critical commercial assays		
Pierce BCA Protein Assay Kit	Thermo Fisher Scientific	Cat#23227
Deposited data		
The LC-MS/MS datasets for proteome profiling of cell conditioned medium (CCM)	This paper	MassIVE / ProteomeXchange with the identifiers MSV000086767 / PXD023839
The LC-MS/MS datasets for proteome profiling of cell-derived matrices (CDM)	This paper	MassIVE / ProteomeXchange with the identifiers MSV000086766 / PXD023833
The LC-MS/MS datasets for proteome profiling of the adhesome	This paper	ProteomeXchange Consortium via PRIDE partner repository with the dataset identifier PXD023821

(*Continued on next page*)

Continued

REAGENT or RESOURCE	SOURCE	IDENTIFIER
Experimental models: cell lines		
Immortalized human podocytes (AB8/13)	M. Saleem, Bristol University	AB8/13
HEK293T/17	ATCC	CRL-11268
Immortalized human podocytes (AB8/13); CRISPR/Cas9 modified; non targeting; *EPB41L5 wild type (WT) clone 1*	Schell et al., 2017	N/A
Immortalized human podocytes (AB8/13); CRISPR/Cas9 modified; non targeting; *EPB41L5 wild type (WT) clone 2*	Schell et al., 2017	N/A
Immortalized human podocytes (AB8/13); CRISPR/Cas9 modified; *EPB41L5* sgRNA-1; *EPB41L5 knockout (KO) clone 1*	Schell et al., 2017	N/A
Immortalized human podocytes (AB8/13); CRISPR/Cas9 modified; *EPB41L5* sgRNA-1; *EPB41L5 knockout (KO) clone 2*	Schell et al., 2017	N/A
Immortalized human podocytes (AB8/13); CRISPR/Cas9 modified; non targeting; *FERMT2, wild type (WT)*	(Yasuda-Yamahara et al., 2018a)	N/A
Immortalized human podocytes (AB8/13); CRISPR/Cas9 modified; *FERMT2* sgRNA-1; *FERTM2 knockout (KO)*	(Yasuda-Yamahara et al., 2018a)	N/A
Immortalized human podocytes (AB8/13); CRISPR/Cas9 modified; pLentiCRISPRv2 non targeting; *EPB41L5 wild type (WT) clone 1*	This paper	N/A
Immortalized human podocytes (AB8/13); CRISPR/Cas9 modified; pLentiCRISPRv2 non targeting; *EPB41L5 wild type (WT) clone 2*	This paper	N/A
Immortalized human podocytes (AB8/13); CRISPR/Cas9 modified; pLentiCRISPRv2 sgRNA-2; *EPB41L5 knockout (KO) clone 1*	This paper	N/A
Immortalized human podocytes (AB8/13); CRISPR/Cas9 modified; pLentiCRISPRv2 sgRNA-2; *EPB41L5 knockout (KO) clone 2*	This paper	N/A
Immortalized human podocytes (AB8/13); CRISPR/Cas9 modified; pLentiCRISPRv2 sgRNA-2; *EPB41L5 knockout (KO) clone 3*	This paper	N/A
Immortalized human podocytes (AB8/13); CRISPR/Cas9 modified; pLentiCRISPRv2 sgRNA-3; *EPB41L5 knockout (KO) clone 1*	This paper	N/A
Immortalized human podocytes (AB8/13); CRISPR/Cas9 modified; pLentiCRISPRv2 sgRNA-3; *EPB41L5 knockout (KO) clone 2*	This paper	N/A
Immortalized human podocytes (AB8/13); CRISPR/Cas9 modified; pLentiCRISPRv2 sgRNA-3; *EPB41L5 knockout (KO) clone 3*	This paper	N/A
Immortalized human podocytes (AB8/13); CRISPR/Cas9 modified; pLentiCRISPRv2 sgRNA-3; *EPB41L5 knockout (KO) clone 4*	This paper	N/A
Immortalized human podocytes (AB8/13); CRISPR/Cas9 modified; TLCV2 non targeting; *PDLIM5 wild type (WT) clone 1*	This paper	N/A
Immortalized human podocytes (AB8/13); CRISPR/Cas9 modified; TLCV2 non targeting; *PDLIM5 wild type (WT) clone 2*	This paper	N/A

(*Continued on next page*)

Continued

REAGENT or RESOURCE	SOURCE	IDENTIFIER
Immortalized human podocytes (AB8/13); CRISPR/Cas9 modified; TLCV2 non targeting; *PDLIM5 wild type (WT) clone 3*	This paper	N/A
Immortalized human podocytes (AB8/13); CRISPR/Cas9 modified; TLCV2 sgRNA-1; *PDLIM5 knockout (KO) clone 1; "KO-1"*	This paper	N/A
Immortalized human podocytes (AB8/13); CRISPR/Cas9 modified; TLCV2 sgRNA-2; *PDLIM5 knockout (KO) clone 1; "KO-2"*	This paper	N/A
Immortalized human podocytes (AB8/13); CRISPR/Cas9 modified; TLCV2 sgRNA-2; *PDLIM5 knockout (KO) clone 2; "KO-3"*	This paper	N/A
Immortalized human podocytes (AB8/13); CRISPR/Cas9 modified; TLCV2 sgRNA-2; *PDLIM5 knockout (KO) clone 3; "KO-4"*	This paper	N/A
Immortalized human podocytes (AB8/13); CRISPR/Cas9 modified; TLCV2 sgRNA-2; *PDLIM5 knockout (KO) clone 4; "KO-5"*	This paper	N/A
Experimental models: organisms/strains		
mouse: *hNPHS2Cre*	Moeller et al., 2003	N/A
mouse: *Epb41l5*$^{flox/flox}$	Schell et al., 2017	N/A
Oligonucleotides		
Oligonucleotides for Genotyping PCR and sgRNA synthesis, see Table S4	This paper	N/A
Recombinant DNA		
Plasmid: TLCV2	Barger et al., 2019	Addgene plasmid #87360
Plasmid: lentiCRISPRv2	Sanjana et al., 2014	Addgene plasmid #52961
Plasmid: pWPXLD	gift from Didier Trono	Addgene plasmid #12258
Plasmid: EPB41L5.pcDNA6	Schell et al., 2017	N/A
Plasmid: Luciferase.pcDNA6	Schell et al., 2017	N/A
Plasmid: EPB41L5-sgRNA2.lentiCRISPRv2	This paper	N/A
Plasmid: EPB41L5-sgRNA3.lentiCRISPRv2	This paper	N/A
Plasmid: PDLIM5-sgRNA1.TLCV2	This paper	N/A
Plasmid: PDLIM5-sgRNA2.TLCV2	This paper	N/A
Plasmid: EGFP.pWPXLd	This paper; swap cloning from existing plasmids Schell et al., 2017	N/A
Plasmid: FLAG.pWPXLd	This paper; swap cloning from existing plasmids Schell et al., 2017	N/A
Plasmid: EPB41L5.pWPXLd	This paper; swap cloning from existing plasmids Schell et al., 2017	N/A
Plasmid: FLAG-EPB41L5.pWPXLd	This paper; swap cloning from existing plasmids Schell et al., 2017	N/A
Software and algorithms		
Fiji Image Analyzer v1.52	FIJI	https://fiji.sc/
Graph Pad Prism 8 Software	GraphPad Software	https://www.graphpad.com/scientific-software/prism/
CHOPCHOP version 2&3	Labun et al., 2019	https://chopchop.cbu.uib.no/
Nephroseq v4	Applied Systems Biology Core, University of Michigan	https://www.nephroseq.org/index.jsp

RESOURCE AVAILABILITY

Lead contact

Further information and requests for resources and reagents should be directed to and will be fulfilled by the Lead Contact, Christoph Schell (christoph.schell@uniklinik-freiburg.de).

Materials availability

Plasmids, cell lines, mouse lines and unique/stable reagents newly generated in this study will be made available on reasonable request (Materials Transfer Agreement (MTA) may be required).

Data and code availability

The LC-MS/MS datasets for proteome profiling of cell-derived matrices (CDM) and cell conditioned medium (CCM) have been made publicly available in MassIVE / ProteomeXchange with the identifiers MSV000086766 / PXD023833 (CDM) and MSV000086767 / PXD023839 (CCM), respectively. The mass spectrometry proteomics data of the adhesome have been deposited to the ProteomeXchange Consortium via the PRIDE partner repository with the dataset identifier PXD023821.

EXPERIMENTAL MODEL AND SUBJECT DETAILS

Animals

Generation of podocyte specific *Epb41l5* knockout (KO) mice was previously described (Schell et al., 2017). In short, the well-established *hNPHS2*-Cre mouse line (Moeller et al., 2003) was intercrossed to *Epb41l5*$^{fl/fl}$ conditional mice to generate a podocyte specific knockout mouse model for *Epb41l5* (the *hNPHS2*-Cre allele was kindly provided by Lawrence Holzman - Renal, Electrolyte and Hypertension Division, University of Pennsylvania School of Medicine Philadelphia, PA, USA). Mice were maintained on a SV129 background. Tissue samples from well-established glomerular disease models (Adriamycin (ADR), and *NWASP* knockout mice) were previously described (Schell et al., 2013, 2015). Mice were housed in a SPF facility with free access to chow (Kliba-NAFAG, standard chow - 3807.PM.L15), water and kept at 12 hour day/night cycle. Animals were housed in groups of 3-5 mice after weaning. Age/developmental stage of animals used for respective experiments are stated in the figures, figure legends and Method details (male and female animals showed similar phenotypes and combined analysis is presented). All mouse experiments were performed according to the National Institutes of Health Guide for the Care and Use of Laboratory Animals, as well as the German law governing the welfare of animals and were approved by local authorities (Regierungspraesidium Freiburg).

Cell Lines

Human immortalized podocyte cells (from male donor) were previously described in detail and maintained according to described procedures (Saleem et al., 2002; Yasuda-Yamahara et al., 2018b). For all cell culture experiments, human immortalized podocytes were cultured in RPMI 1640 medium supplemented with Glutamine, 10% FCS, ITS and non-essential amino acids. Podocytes were cultured in RPMI in a cell culture incubator at 33°C, 95% air 5% CO_2. Humane HEK293T/17 cells were cultured in Dulbecco's Modified Eagle's Medium supplemented with Glutamine and 10% FCS. HEK293T/17 cells (from female donor) were cultured in a cell culture incubator at 37°C, 95% air 5% CO_2. The used human immortalized podocyte cell line was created and received from M. Saleem, Bristol University (Saleem et al., 2002). Authentic HEK293T/17 cells were purchased at ATCC. Therefore no further authentication was performed.

METHOD DETAILS

Experimental Design

Number of independent experiments and total amount of analyzed cells, mice or samples are stated in the figures and/or figure legends. Samples were not randomized or blinded for quantification and analysis.

Glomerular Preparation

Isolation of glomeruli from 3 week old mice was performed based on perfusion with magnetic beads (Dynabead) as previously described in detail (Boerries et al., 2013). Glomeruli were glass-glass homogenized in RIPA lysis buffer (containing 20 mM CHAPS, Proteinase and Phosphatase inhibitors) and centrifuged at 15000 g for 15 minutes at 4°C. Protein concentrations were assessed using Pierce BCA Protein Assay Kit (Thermo Fisher Scientific, Waltham, USA) and equal amounts of protein were applied for SDS-PAGE.

Antibodies

Application of antibodies used in this study was described in detail in the respective method sections and in Table S3.

SEM, TEM and CLEM Procedures

Preparation of kidney samples for transmission electron microscopy (TEM) was performed as previously described (Schell et al., 2018). In brief, small pieces of the renal cortex were dissected and cubes of about 2x2x2 mm were cut using razor blades. Samples were transferred into glass vials and immersion fixated using 4% PFA and 1% GA in PBS overnight at 4°C. The tissue was post-fixed in 1% osmium tetroxide in 6,86% saccharose in 0,1M phosphate buffer for 30 min and washed 6 times in 0,1M phosphate buffer. Dehydration was performed by 15 min incubations in 30% ethyl alcohol (EtOH) and 50% EtOH. The tissue was incubated in 1% uranyl acetate in 70% EtOH overnight at 4°C and further dehydrated in increasing concentrations of EtOH and finally aceton. After embedding in Durcupan resin ultrathin sections were cut using a UC7 Ultramicrotome (Leica), collected on Formvar-coated copper grids. Post staining was done for 1min with 3% Lead Citrate followed by imaging using a Zeiss Leo 912 transmission electron microscope. Embedding, semi-thin sectioning and electron microscopy was performed at the EM core facility of the Department of Nephrology, Faculty of Medicine, University of Freiburg.

For correlative light-electron microscopy (CLEM), immunofluorescence (IF) and scanning electron microscopy (SEM) was performed sequentially. Maximum intensity projections of IF images were correlated to SEM images using Fiji ImageJ v1.51 s software (National Institute of Health (NIH), Bethesda, USA). Preparation of SEM samples was previously described (Schell et al., 2018). Electron microscopy was performed at the EM core facility of the Department of Nephrology, Faculty of Medicine, University of Freiburg.

Histology and Immunofluorescence Staining of Kidney Sections

Immunofluorescence staining of frozen kidney sections was performed as previously described (Schell et al., 2017). In brief, 4 μm sections were fixed in 4% PFA for 3 minutes and blocked with 5% BSA in PBS before primary antibodies were applied. After repetitive washing, sections were incubated with fluorophore-conjugated secondary antibodies. Following antibodies were used: NPHS1 (GP-N2, Progen), COL4 (ab6586, Abcam), LAMB1 (Jeffrey Miner, Washington University in St. Louis; Sasaki et al., 2002), COL4A4 (Jeffrey Miner, Washington University in St. Louis; Miner and Sanes, 1994). For COL4A4 fixation with 100% ethanol and pre-treatment with urea-glycine solution (6 M urea and 0,1 M glycine in ddH_2O, pH 3,5) was performed as previously described (Miner and Sanes, 1994). Glomerular COL4A4 expression was quantified using Fiji ImageJ. Tuft areas of NPHS1 positive glomeruli were manually selected and mean fluorescence intensities per tuft area were measured for COL4A4. 21-57 glomeruli per animal were analyzed.

Kidney sections (2 μm) of FFPE tissue were generated as previously described (Schell et al., 2018). Afterward, sections were deparaffinized, rehydrated and underwent heat-induced antigen retrieval (Tris-EDTA buffer pH9, 15 minutes, pressure cooker). Sections were subsequently blocked with 5% BSA in PBS, incubated with primary antibodies and processed for immunofluorescence staining as described above. Following antibodies were used: PDLIM5 (HPA016740, Atlas Antibodies), EPB41L5 (HPA037564, Atlas Antibodies), NPHS1 (GP-N2, Progen), WT1 (ab15249, Abcam). Podocytes per glomeruli were quantified from clearly NPHS1 positive glomeruli at p0 (to ensure analysis of only late capillary lope and mature glomerular developmental states). All glomeruli fulfilling these criteria (9-31 per kidney section and animal) were analyzed. Cells with double positivity for NPHS1 and WT1 were identified as podocytes and podocyte numbers per tuft area and glomerulus were calculated.

Microscopy

Immunofluorescence images were taken with an inverted Zeiss Axio Observer microscope equipped with an ApoTome.2, an Axiocam 702 mono and Colibri 7 illumination system. In addition an inverted Zeiss Axio Imager microscope was used. 100x, 63x, 40x, 20x and 10x objectives with Zeiss fluorescence filter sets (49 DAPI, 38 GFP, 43 HE dsRed, 50 Cy5) were used for immunofluorescence and 40x and 20x objectives for phase-contrast analysis.

CRISPR/Cas9

For cell culture experiments established *EPB41L5* knockout and wild-type podocyte cell lines were used (referred to as KO-1, KO-2, WT-1, WT-2). Generation, validation, and characterization of these cell lines were described before (Schell et al., 2017). In brief, KO cells were generated using CRISPR/Cas9 genome editing technology in human immortalized podocytes. gRNA-1 was subsequently cloned in a CRISPR nuclease vector according to the manufacturer's instructions (gRNA-1: 5′-GACTTAGAATCTCCAGCTGC(AGG)-3′, gene-art, Invitrogen, Karlsruhe, Germany). Single cell clones were validated using Sanger sequencing and western blot analysis. CRISPR/Cas9 genome edited *FERMT2* KO podocytes were previously described (Yasuda-Yamahara et al., 2018a). *EPB41L5* WT-1 control was generated from crude podocyte cell culture transfected with empty vector. *EPB41L5* WT-2 control and *FERMT2* WT control was generated from non-mutated podocyte clones.

For generating further *EPB41L5* KO and *PDLIM5* KO cell lines gRNAs were designed using the web-based platform CHOPCHOP (Labun et al., 2019) (*EPB41L5* gRNA-2: 5′- CTTACCGGAACAATCCACCG(GGG)-3′, *EPB41L5* gRNA-3: 5′-GGACACCCGACACGTG ATGA(TGG)-3′, *PDLIM5* gRNA-1: 5′- GATGTGCGCCCATTGTAACC(AGG)-3′, *PDLIM5* gRNA-2: 5′- ATACTGAAGACTGGCGTCC A(AGG)-3′). *EPB41L5* gRNAs were further subcloned in a lentiCRISPRv2 plasmid which was a gift from Feng Zhang (Addgene plasmid #52961; http://addgene.org/52961; RRID:Addgene_52961; Sanjana et al., 2014). *PDLIM5* gRNAs were further subcloned in a modified lentiCRISPRv2 plasmid (TLCV2) which was a gift from Adam Karpf (Addgene plasmid #87360; http://addgene.org/87360; RRID:Addgene_87360; Barger et al., 2019). Control (WT) clones were generated by using the lentiCRISPRv2 and TLCV2 plasmid without gRNA sequence for each individual gRNA respectively. Human immortalized podocytes were transduced with lentiviral particles and single cell clones were generated. *EPB41L5* KO clones were validated by western blot analysis.

EPB41L5 Expression Constructs

EGFP, human full length *EPB41L5* and n-terminal FLAG tagged *EPB41L5* were swap-cloned into the pWPXLD plasmid which was a gift from Didier Trono (Addgene plasmid #12258; http://addgene.org/12258; RRID:Addgene_12258). Plasmids were validated by Sanger sequencing. Lentiviral transfection was performed and protein expression was validated by western blot analysis.

Preparation and Staining of CDMs

For synthesis of cellular derived matrices (CDMs) podocytes were seeded for 7 or 14 days on gelatin-coated (mainly consisting of collagen I) coverslips on 24 well plates. The podocyte medium was supplemented with 50 μg/ml vitamin C and changed every 24 hours. To analyze the decellularized CDMs cells were removed by an optimized preparation technique as previously described (Kaukonen et al., 2017). In brief, cells were incubated with pre-warmed (37°C) extraction buffer (0,5% Triton X-100 and 20 mM NH_4OH in PBS) for 3 minutes at room temperature. The cellular debris was diluted and removed by gently washing two times with PBS. Next, DNase I solution (15 U/ml DNase I and 1mM $CaCl^{2+}MgCl^{2+}$ in PBS) was added and incubated for 30 min at 37°C to eliminate residual cellular DNA. After this incubation the enzyme was removed and the CDMs were carefully washed three times with PBS. The resulting decellularized CDMs were used for further analysis. For visualization of native CDMs cells were seeded on collagen IV coated coverslips, CDMs were generated as described above and then fixed without any decellularization procedures.

Immunofluorescence staining of decellularized and native CDMs was performed via fixation with 4% PFA for 20 minutes and further incubation with 50 mM NH_4Cl in PBS for 7min. After repetitive washing with PBS, permeabilization with 0,1% Triton X-100 in PBS was performed for 3min. Then the CDMs were blocked with 5% BSA in PBS for 1 hour and incubated with COL4A2 (MAB1910, Merck KGgA) for 2 hours. After several washing steps the fluorophore-conjugated secondary antibodies were applied for 1 hour.

Immunofluorescence staining of CDMs with LAMA5 (AMAb91124, Atlas Antibodies), LAMC1 (HPA001909, Atlas Antibodies) and COL4 (ab6586, Abcam) was performed after heat-induced antigen retrieval (Tris-EDTA buffer pH9, 30min, steamer). Subsequent staining procedures were performed as described before.

Inhibition studies were performed by adding 1 μM Marimastat in DMSO (Selleckchem, Munich, Germany) or 20 μM Y27632 in DMSO (Selleckchem, Munich, Germany) to the podocyte medium supplemented with 50 μg/ml vitamin C over 7 days of CDM generation. Medium was also changed every 24 hours.

Quantitative Analysis of CDMs

CDMs were analyzed by electron microscopy, immunofluorescence staining, western blot and proteomics as stated in the respective method sections. Quantitative analysis of CDMs was based on COL4A2 and DAPI immunofluorescence staining. CDM scores of decellularized CDMs were quantified employing analysis of the fibrillary networks and structures as shown in Figure S4. A semiquantitative score (5-tier grade) was defined (grade 0: one layer of not interacting and no or very short fibers; grade 1: one layer of week interacting and short fibers; grade 2: 2 layers of interacting fibers and few fiber bundles; grade 3: > 2 layers of interacting fibers and fiber bundles building a thin fiber network; grade 4: multiple layers of strong interacting fibers and fiber bundles building a dense fiber network), 15 high power fields (200x magnification) per sample/replicate were analyzed and the mean score per sample/replicate was calculated. ECM thickness was measured using native CDMs without any decellularization or gelatin coating procedures. Therefore, the focal distance between the top and bottom plain of the CDM/cell sheet was measured using the z stack function of the ZEISS ZEN2 software.

LAMA5 and LAMC1 binding to Collagen IV fibers was quantified using Fiji ImageJ. First, immunofluorescence images were acquired using a 100x objective, z stack and apotome function of the AxioImager microscope. Z stacks were converted to maximum intensity projections (MIPs) and Collagen IV fibers were selected by thresholding the COL4 or COL4A2 immunofluorescence signal respectively. LAMA5 or LAMC1 positive regions were segmented and within this Collagen IV mask the ratio of Laminin positive to total Collagen IV fiber area was calculated per individual image.

Cell Adhesion Assay

Cell adhesion assays were performed on different extracellular matrix components as previously described (Humphries, 2009). Collagen IV (50 μg/ml, collagen from human placenta, Merck, Darmstadt, Germany), collagen I (50 μg/ml, PureCol, Advanced BioMatrix, San Diego, USA), fibronectin (50 μg/ml, human fibronectin, Corning Inc., New York, USA) and several laminins (5 μg/ml, Biolaminin LN, BioLamina, Sundbyberg, Sweden) were used as indicated. Briefly, 24 well cell culture plates were coated according to the manufacturer's instructions and blocked with heat-denatured BSA (1% in PBS). Cells were trypsinized, counted and equal amounts of cells were seeded for 15 minutes on precoated 24 well cell culture plates. After several washing and fixation in 4% PFA, adherent cells were stained with 0,1% crystal violet in ddH_2O for 1 hour. The dye was solubilized, and absorbance was measured at 570nm using a microplate reader.

For cell adhesion assays on CDMs *EPB41L5* WT and KO cells were seeded without any coating or with precoating as indicated (0,2% gelatin (mainly consisting of collagen I) or laminin-521 5 μg/ml) on 24well cell culture plates and CDMs were generated over a period of 7 days. After decellularization cell adhesion assays were performed using equal amounts of WT cells as described above.

Co-Culture Experiments

Co-culture experiments were performed using *EPB41L5* WT and KO cells. For free exchange of soluble factors cells were seeded on ibidi μ-slide well co-culture dishes (Ibidi GmbH, Gräfelfing, Germany) with *EPB41L5* WT and KO cells as recipient or feeder cells. For direct cellular interaction cells were seeded on gelatin-precoated (mainly consisting of collagen I) coverslips on 24 well cell culture plates in various combinations (100% WT, 75% WT + 25% KO, 50% WT + 50% KO, 100% KO). CDMs were generated over a period of 7 days, decellularized and immunofluorescence-stained as described above.

CDM Reseeding Assay

CDMs were generated on 3.5 cm cell culture dishes Advanced TC (Greiner Bio-One International GmbH, Kremsmünster, Austria) without any precoating. Cells were seeded and CDMs were synthesized over a period of 7 days as described before. CDMs were decellularized and WT cells were seeded and incubated for 3 hours. Afterward the dishes were washed with PBS and fixed with 4% PFA. For analyzing Myosin-II-activity, YAP/TAZ nuclear translocation and morphological features immunofluorescence staining was employed as described before. Following antibodies were used: pMLC (#3671, Cell Signaling), pMLC (#3674, Cell Signaling), YAP/TAZ (#8418, Cell Signaling). Fluorescence intensities (gray values) were quantified from images using Fiji ImageJ. For pMLC analysis cell bodies were segmented based on Phalloidin (F-Actin) co-staining. For YAP/TAZ analysis cell nuclei were segmented based on DAPI co-staining.

Western Blot Analysis

Western Blot analysis was performed using whole cell lysates, CDM lysates and CM lysates. Whole cell lysates were generated via scraping the cells in RIPA buffer following denaturation with 2xLaemmli buffer with DTT. CDMs of *EPB41L5* WT and KO cells were generated on 10 cm dishes without any precoating over a period of 7 days and subsequently decellularization was performed as described above. CDMs were then scraped in 2xLaemmli buffer with DTT and denatured for 20 min at 70°C followed by 5 min at 95°C. For generation of conditioned media (CM), *EPB41L5* WT and KO cells were seeded on 14.5 cm Advanced TC dishes (Greiner Bio-One International GmbH, Kremsmünster, Austria) and cultured for 5 days. The medium was supplemented with 50 μg/ml vitamin C and changed every 48 hours. Hereon cells were washed 3 times and subsequently RPMI without FCS and phenol red (supplemented with ITS, non-essential amino acids and vitamin C) was added. CM was harvested after 24 hours, centrifuged (3000 g, 5 min, room temperature), filtered (0.45 μm filter) and then concentrated via Pierce Protein Concentrator columns (Thermo Fisher Scientific, Waltham, USA).

Digestion of generated CDMs was performed using Collagenase (preparation type 2, Worthington Biochemical Corp., Lakewood, USA). In brief, CDMs of *EPB41L5* WT and KO cells were generated on 10 cm dishes without any precoating over a period of 7 days and subsequently scraped in HBSS containing 1 mM $CaCl^{2+}MgCl^{2+}$ and 1 mg/ml Collagenase. After an incubation of 2 hours at 37°C while gently shaking, samples were centrifuged (20000 g for 10 min at 4°C) and denatured for 5 min at 95°C by adding 2xLaemmli with DTT.

Protein concentration was measured using the Pierce BCA Protein Assay Kit (Thermo Fisher Scientific, Waltham, USA) following the manufacturer's instructions. Equal amounts of protein or equal percentage of totally generated CDMs were loaded for standard SDS-polyacrylamide gel electrophoresis (SDS-PAGE) or for Coomassie staining. Coomassie staining was performed according to the manufacturer's instructions (Imperial Protein Stain, Thermo Fisher Scientific).

SDS-PAGE and western blotting was performed using standard procedures. Blots were imaged using the HRP/ECL chemiluminesce method and X-ray films. For western blot validation of *PDLIM5* KO podocytes a Chemiluminescence Imager (Intas) was used for digital image acquisition. Densitometry quantification of blot bands was performed using Fiji ImageJ.

Immunoprecipitation

Cells were cultured on 14.5 cm dishes to 90% confluency. Subsequently cells were lysed in Triton X-100 lysis buffer (1% Triton X-100, 20mM Tris-HCL, 50mM NaCl, 50mM NaF, 15mM $Na_4P_2O_7$, 1mM EDTA in ddH_2O, pH 7,4) supplemented with proteinase and phosphatase inhibitors and centrifuged. Supernatants were incubated for 1 hour at 4°C with Anti-FLAG M2 Affinity Agarose Gel (Merck, Darmstadt, Germany). Subsequently four wash steps with Triton X-100 lysis buffer were performed. Bound proteins were resolved in 2xLaemmli buffer with DTT and denatured at 95°C for 5 min. Lysates were separated and analyzed by standard SDS-PAGE.

Focal Adhesion Analysis

EPB41L5 WT and KO cells were seeded on collagen IV coated 8 well μ-Slides (Ibidi GmbH, Gräfelfing, Germany) for PXN and ZYX analysis or on 50μg/ml collagen IV coated (collagen from human placenta, Merck, Darmstadt, Germany) 3.5 cm glass bottom dishes (Ibidi GmbH) for PDLIM5 and ACTN4 analysis. Podocytes were cultivated overnight for achieving steady state condition. Cells were fixed in 4% PFA and subsequently immunofluorescence staining for focal adhesion proteins (PXN, ZYX, PDLIM5 and ACTN4) was applied as described above. Substrate stiffness dependent focal adhesion maturation was analyzed using 3.5 cm μ-dishes ESS 1,5kPa (Ibidi GmbH) and 3.5 cm glass bottom dishes (Ibidi GmbH). Cell culture dishes were precoated with fibronectin (25 μg/ml,

human fibronectin, Corning Inc., New York, USA). Cells were incubated overnight before fixation and subsequent immunofluorescence staining was employed as described above. For Inhibition studies 10 μM Y27632 in DMSO (Selleckchem, Munich, Germany) was applied for 1 hour. Following antibodies were used: PXN (610051, BD Biosciences), ZYX (HPA004835, Atlas Antibodies), ACTN4 (ab108198, Abcam), PDLIM5 (HPA016740, Atlas Antibodies). Analysis of focal adhesions was performed using an image processing macro for Fiji ImageJ as described before (Schell et al., 2018). In brief, individual focal adhesions (FA) were segmented based on PXN immunofluorescence signal. Therefore, images were processed via background subtraction, unsharp masking, binarization and selection of binary FAs. This FA mask was transferred to the unprocessed image and segmented individual FAs were analyzed for morphometric parameters. ZYX, ACTN4 or PDLIM5 intensity of FAs was analyzed by using this PXN based FA mask in PXN co-stained cells. In addition, morphometric parameters of respective cells were measured to calculate FA density and the percentage of FA covered cell area for individual cells. Substrate stiffness dependent FA recruitment of ACTN4 and PDLIM5 was quantified applying a semiquantitative score (3 grades: strong, medium, low) on whole cell level to avoided fluorescence intensity artifacts by substrate gels. 100 cells per condition and replicate were quantified using a fluorescence microscope and 40x objective).

Traction Force Microscopy

Traction force microscopy (TFM) was performed as previously described (Plotnikov et al., 2014; Schell et al., 2018). In brief, gels with a Young's modulus of 16kPa PAA (poly-acrylamide) were prepared on ibidi glass bottom μ-dishes. Gels were crosslinked to 1 mg/ml fibronectin for 4h after gel activation by the SulfO-SANPAH cross-linker. Equal amounts of cells per dish were seeded and cultivated at 37°C for 24 hours before the measurement of forces. Images of respective cells and subcellular beats were recorded before and after removal of the cell. Manipulation of the cells was performed with a micromanipulator (Eppendorf). Image analysis was done as previously described (Plotnikov et al., 2014).

Collagen Bundling Assay

PurCol collagen I gels (Advanced BioMatrix, San Diego, USA) were polymerized on 3.5 cm glass bottom dishes (Ibidi GmbH, Gräfelfing, Germany) according to the manufacturer's instructions. *EPB41L5* WT and KO cells were seeded and incubated overnight. Cells were subsequently fixed in 4% PFA and immunofluorescence staining was applied as described before using a COL1 antibody (NB600-408, Novus Biologicals).

Proteomics Procedures

For MS analysis of the podocyte secretome, sample generation was performed as described above for conditioned media (CM). After harvesting, CM was supplemented with 10 mM EDTA and 1 mM PMSF. Samples were centrifuged (3000 g, 5 min, 4°C) and filtered (0.22 μm filter). Proteins were precipitated from CM using Trichloroacetic acid (TCA). For label free quantitative proteomic analyses, sample preparation and mass spectrometry analysis (Q-Exactive plus system, Thermo Scientific, Bremen, Germany) were performed as previously reported (Biniossek et al., 2016). LC-MS/MS data analysis was performed as reported before (Biniossek et al., 2016).

For MS analysis of the podocyte matrisome, CDMs were generated according to the protocol described above. SILAC labeling of human immortalized podocytes was performed for 14 days as previously described (Schell et al., 2017). Thereafter SILAC medium supplemented with 50 μg/ml vitamin C was used to generate CDMs without any precoating procedures. After decellularization, CDMs were scraped into RIPA buffer, centrifuged, protein concentration was determined and 6xLaemmli buffer (+DTT) was added followed by denaturation at 70°C for 20 min. Based on SILAC labeling and protein concentration WT and KO samples were mixed 1:1 for MS-analysis.

For MS analysis of the podocyte adhesome, *EPB41L5* or Luciferase (as negative control) was transiently expressed in SILAC labeled podocytes by nucleofection (Amaxa Nucleofector, Lonza, Switzerland). Podocytes were seeded on cell culture dishes for 24 hours. Isolation of integrin adhesion complexes from podocytes was performed as previously described (Schell et al., 2017; Rogg et al., 2017). MS analysis of SILAC labeled samples was performed as previously described (Schell et al., 2017).

Matrisome and secretome datasets were compared to "The Matrisome Project" database for selection of consensus matrisome components (Hynes and Naba, 2012; Naba et al., 2016).

QUANTIFICATION AND STATISTICAL ANALYSIS

If not stated otherwise in the figure legends, data are expressed as mean ± SEM. Scatter dots indicating individual data points were used for statistical analysis. Violin plots (Figures 4G and 5F) were used to visualize data distribution of FA sizes by means of the probability density of single FAs at different FA size values. In Figure 4G the white dot on the violin plot indicates the median, black bar indicates the interquartile range and whiskers indicate the lower/upper adjacent values (1.5x interquartile range). In Figure 5F lines indicate the median and quartiles.

Statistic tests were used based on data distribution and experimental design. The following tests were used for indicated experiments: Unpaired Student's t test (Figures 4A, 4J, 5I, and 5K), Unpaired t test with Welch's correction (Figures 1C, 1F, 3G, 5B, 5C, 5D, and 6H), Mann-Whitney-U-test (Figure 5F), ONE-WAY Anova with Tukey's multiple comparisons test) (Figures 1L, 1M, 1N, 2I, 2J,

3C, 3I, 3K, 4D, 4E, 4F, 4H, 4I, and 6C) or TWO-WAY Anova with Sidak's multiple comparisons test (Figure 6E, only p values for strong recruitment are shown).

GraphPad Prism 8 software was used for statistical testing. The Nephroseq v4 database (https://www.nephroseq.org) was used for statistical analysis of *EPB41L5* expression in human glomerular disease (Table S2). Statistical significance was defined as *$p < 0.05$, **$p < 0.01$, ***$p < 0.001$ and ****$p < 0.0001$, n. s. – non-significant. Number of independent experiments and total amount of analyzed cells, mice or samples are stated in the figures and/or figure legends.

Cell Reports, Volume *34*

Supplemental information

EPB41L5 controls podocyte extracellular matrix assembly by adhesome-dependent force transmission

Jasmin I. Maier, Manuel Rogg, Martin Helmstädter, Alena Sammarco, Oliver Schilling, Benedikt Sabass, Jeffrey H. Miner, Jörn Dengjel, Gerd Walz, Martin Werner, Tobias B. Huber, and Christoph Schell

Supplementary Figure Legends

Supplemental Figure 1. Analysis of *Epb41l5*$^{fl/fl}$**NPHS2Cre* mice. Related to Figure 1.

(a) Re-analysis of *in vivo* proteome data sets and comparison with podocyte specific marker proteins validates EBP41L5 as a highly podocyte specific enriched protein (Schell et al., 2017, Rinschen et al., 2018). (b) Correlative light/electron microscopy (CLEM) demonstrates predominant localization of EPB41L5 in the basal compartment of murine podocytes (maximum intensity projections (MIP) of z-stacks are shown; white arrows indicate co-localization; co-staining with NPHS1 marks podocytes). (c-d) Immunofluorescence staining demonstrates loss of EPB41L5 in the podocyte compartment of respective *Epb41l5*$^{fl/fl}$**NPHS2Cre* KO mice (NPHS1 was employed as a podocyte specific co-marker). EPB41L5 expression in parietal epithelial cells (PECs) was not affected by podocyte specific deletion of *Epb41l5* (indicated by white arrowheads). (e) PAS staining of glomeruli of *Epb41l5*$^{fl/fl}$**NPHS2Cre KO* or WT mice (black arrow indicate GBM thickening; black arrowhead indicates areas of mesangial expansion). (f) Immunofluorescence staining of WT1 and NPHS1 shows no significant (n.s.) loss of WT1 and NPHS1 positive podocytes from glomeruli at p0 (scattered dots indicate individual animals). Data are represented as mean ± SEM.

Supplemental Figure 2. Electron microscopy analysis of *Epb41l5*$^{fl/fl}$**NPHS2Cre* mice. Related to Figure 1.

(a) Ultrastructural analysis employing transmission electron microscopy (SEM) shows impaired BM fusion and accumulation of inhomogeneous ECM material in *Epb41l5* $^{fl/fl}$**NPHS2Cre* KO mice at p0 (white box indicates subepithelial ECM accumulation; white arrows indicate GBM invasive cellular protrusions; red arrows mark subepithelial GBM outpocketing; asterisks indicate accumulation of fibrillary ECM structures). (b) Foot process (FP) to endothelial cell (EC) distance was quantified at p0 (scatter dot plots indicate individual glomeruli; 5 WT and 5 KO mice and 1-6 glomeruli per mouse were analyzed; ****p<0.0001). Corresponding mean distance per analyzed mouse is shown in main Figure 1. (c) Fraction of unfused BM (expressed as percentage in relation to total analyzed GBM; scatter dots indicate individual glomeruli; 5 WT and 5 KO mice and 1-6 glomeruli per mouse were analyzed; *p<0.05). (d) Analysis of the glomerular basement membrane (GBM) by TEM revealed pathological remodeling of the GBM and persistence of unfused endothelial and epithelial BMs in *Epb41l5* $^{fl/fl}$**NPHS2Cre* KO mice at p7 (black arrows indicate GBM in WT animals; black arrowheads mark epithelial BM and white arrowheads mark endothelial BM; white asterisks indicate accumulation of fibrillary ECM; red arrow marks subepithelial GBM outpocketing; FP – foot process, EC – endothelial cell). Data are represented as mean ± SEM.

Supplemental Figure 3. GBM immunofluorescence analysis of *Epb41l5*$^{fl/fl}$NPHS2Cre* mice. Related to Figure 1.**

(a) Images corresponding to analysis in main Figure 1. Immunofluorescence analysis of COL4A4 was performed in kidneys of *Epb41l5* $^{fl/fl}$**NPHS2Cre* KO and WT mice at p21 (red arrows indicate areas of decreased COL4A4 staining). (c-f) Immunofluorescence analysis of collagen IV (COL4) and LAMB1 was performed in glomeruli of *Epb41l5* $^{fl/fl}$**NPHS2Cre* KO and WT mice at p21. The basal podocyte compartment was co-stained with NPHS1 (boxed regions indicate zoomed-in detail; yellow arrows indicate areas of aberrant accumulation of COL4 and LAMB1 in the GBM of *Epb41l5* $^{fl/fl}$**NPHS2Cre* KO mice. (g-h) Immunofluorescence analysis of glomerular COL4A4 expression demonstrates no significant changes in expression levels in KO mice at p0 (each dot indicates one individual animal; 21-57 glomeruli per mouse were analyzed; n.s. - non-significant). Data are represented as mean ± SEM.

Supplemental Figure 4. ECM analysis and validation of *EPB41L5* CRISPR/Cas9 cells. Related to Figure 1.

(a) Exemplary images illustrating scoring of ECM structure employing a semiquantitative score (5-tier grade). Fibrillary ECM was stained by COL4A2 (lower panels show zoomed-in details; intensities were transformed to gold LUT as indicated by intensity chart). (b-e) Western blot analysis of *EPB41L5* CRISPR/Cas9 KO and WT clones confirms loss of EPB41L5 in respective KO clones (GAPDH (Glycerinaldehyd-3-phosphat-Dehydrogenase) and alpha-tubulin (TUBA) were employed as a reference housekeeping protein). ECM analysis demonstrates impaired COL4A2 network integrity in all clones. (c) Semiquantitative ECM-scoring demonstrates impaired COL4A2 network integrity due to loss of EPB41L5 after 14 days of CDM synthesis. Corresponding to analysis in Figure 1g-n, *EPB41L5* KO podocytes showed no further improvement in COL4 network at 14 days compared to 7 days of CDM synthesis (4 independent replicates per condition were analyzed; ****p<0.0001). (e) Representative images of decellularized CDMs of *EPB41L5* WT and KO clones generated from gRNA2 and gRNA3 (fluorescence intensities were transformed to gold LUT as indicated by intensity chart). (f) Western blot analysis of *EPB41L5* KO podocytes confirms stable re-expression of EPB41L5 or EGFP (control). (g-h) COL4A2 immunofluorescence analysis of de-cellularized ECM demonstrates increased COL4 network density in matrices of *EPB41L5* rescue podocytes (fluorescence intensities were transformed to gold LUT as indicated by intensity charts). Semi-quantitative ECM-scoring of CDMs synthesized over 7 days (scatter dots indicate individual KO+EGFP (pooled KO1+EGFP&KO2+EGFP) and KO+EPB41L5 (pooled KO1+EPB41L5&KO2+EPB41L5) samples; 2 replicates for each genotype were analyzed; ****p<0.0001). Data are represented as mean ± SEM.

Supplemental Figure 5. Analysis of *EPB41L5* dependent CDMs. Related to Figure 2&3.

(a) Global correlation analysis for secretome and matrisome datasets indicating no overall or direct relation of altered soluble and insoluble ECM proteins (a-1 - 299 proteins detected in both datasets; a-2 - 56 consensus ECM proteins detected in both datasets; pearson`s correlation coefficient was calculated). (b) Application of the broad spectrum MMP inhibitor Marimastat does not ameliorate *EPB41L5*-dependent structural ECM phenotypes (fluorescence intensities were transformed to gold LUT as indicated by intensity chart; MIPs of z-stacks are shown). (c) Additional CDM immunofluorescence staining for COL4A2 corresponding to experiments shown in Figure 2g-j. (d) Coomassie blue staining of unbalanced total protein preparations from conditioned media (CM) or cellular derived matrices (CDM). (e) Western blot analysis for Cortactin (CTTN) demonstrates successful enrichment of extracellular proteins in CMs and CDMs with minimal contamination of intracellular proteins. (f) Western blot quantification of LAMC1 and COL4 levels in CM of *EPB41L5* WT and KO podocytes. Analysis corresponding to Figure 3d (scatter dots indicate individual CM preparations from WT-1, WT-2, KO-1 and KO-2 clones, *p<0.05; **p<0.01). Data are represented as mean ± SEM.

Supplemental Figure 6. Functional analysis of *EPB41L5* dependent CDMs. Related to Figure 3.

(a) Immunofluorescence analysis of collagen IV and laminin chains confirms decreased incorporation of COL4A2 and LAMC1 in filamentous ECM of *EPB41L5* KO podocytes (overview images). Laminin was predominantly detected attached to collagen IV filaments (boxed regions indicate zoomed-in detail). (b) Quantification of LAMC1 recruitment to collagen IV fibers (dots indicate analyzed MIPs of 88x66µm micrographs; ***p<0.001). (c-d) Cell spreading of WT podocytes on *EPB41L5* KO and WT CDMs reveals morphological simplification of WT podocytes on KO CDMs. Cell morphology was visualized by F-actin (Phalloidin) staining and analyzed by measurement of cell circularities (n=4 independent experiments and 200 podocytes per group; ****p<0.0001). (e-f) Detailed analysis of spread WT cells reveals decreased cellular protrusions on KO CDMs (arrowheads indicate filopodia and lamellipodia, boxed regions indicate zoomed-in details, gamma adjusted MIPs are shown for better visualization of filopodia). (g-h) Spread WT podocytes show increased phosphorylated myosin light chain (pMLC) intensity levels on KO CDMs (pMLC depicted in red, F-actin (Phalloidin) in green; boxed regions indicate zoomed-in details; arrowheads indicate altered actomyosin filament distribution; 50 cells on WT or KO CDMs were analyzed; values were normalized to the mean of WT; ****p<0.0001). (i-j) Spread WT podocytes show increased nuclear YAP/TAZ translocation on KO CDMs (YAP/TAZ shown in red, F-actin (Phalloidin) in green, cell nucleus (DAPI) in blue; arrowheads indicate cell nuclei; 87 WT and 87 KO cells were analyzed; values were normalized to the mean of WT; ****p<0.0001). Data are represented as mean ± SEM.

Supplemental Figure 7. Analysis of *EPB41L5* dependent IAC function and composition. Related to Figure 5, 6 and 7.

(a) Application of the ROCK inhibitor Y27632 (10 µM) decreases incorporation of LAMC1 and LAMA5 into filamentous collagen IV ECM. Collagen IV fibers were co-stained with COL4A2 and COL4 (MIPs of z-stacks are shown). (b) Western blot analysis of *EPB41L5* WT and KO podocytes demonstrates unaltered expression of PDLIM5 and ACTN4 in KO podocytes (lysates were balanced to protein concentration as validated by TUBA and GAPDH). (c) Immunoprecipitation of EPB41L5 demonstrates association of EPB41L5 with alpha-Actinin (pan-ACTN), ACTN4 and PDLIM5, whereas other adhesion proteins do not interact with this complex (e.g. ZYX, VASP). (d) Expression of *EPB41L5*, *ACTN4* and *PDLIM5* is significantly downregulated in glomerular disease entities like diabetic nephropathy (DN), focal segmental glomerulosclerosis (FSGS), collapsing FSGS (cFSGS) and lupus nephritis. Alterations in minimal change disease (MCD) were not significant. For details and analysis of Nephroseq disease datasets see supplementary table 2. (e) EPB41L5 and PDLIM5 immunofluorescence signal is depleted from glomeruli at advanced disease stages. Glomeruli of mice with Adriamycin (ADR) induced glomerulopathy as well as a podocyte specific genetic FSGS model were analyzed. Advanced glomerular disease stage is indicated by loss of NPHS1 staining.

Supplemental Figure 1

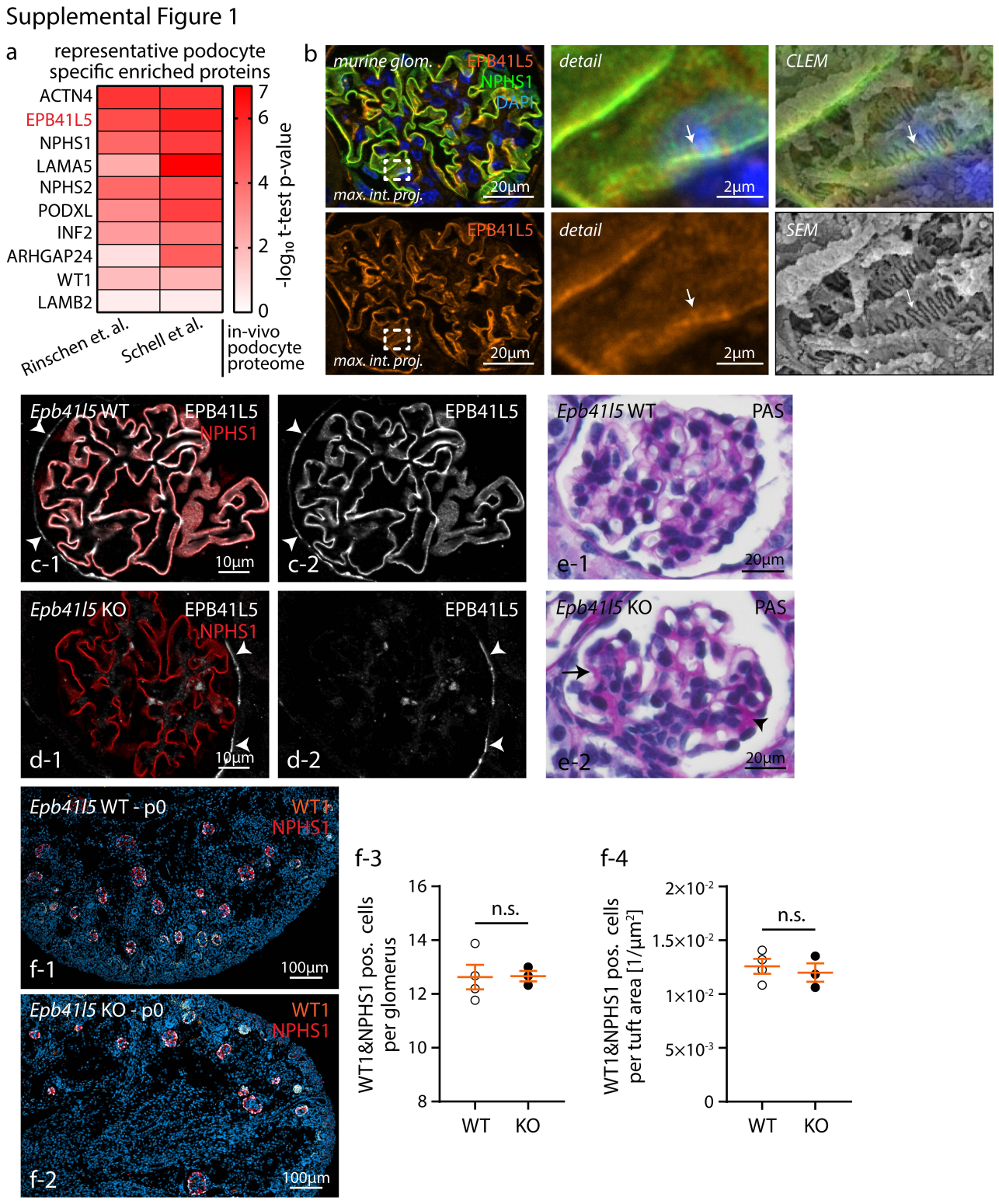

Supplemental Figure 2

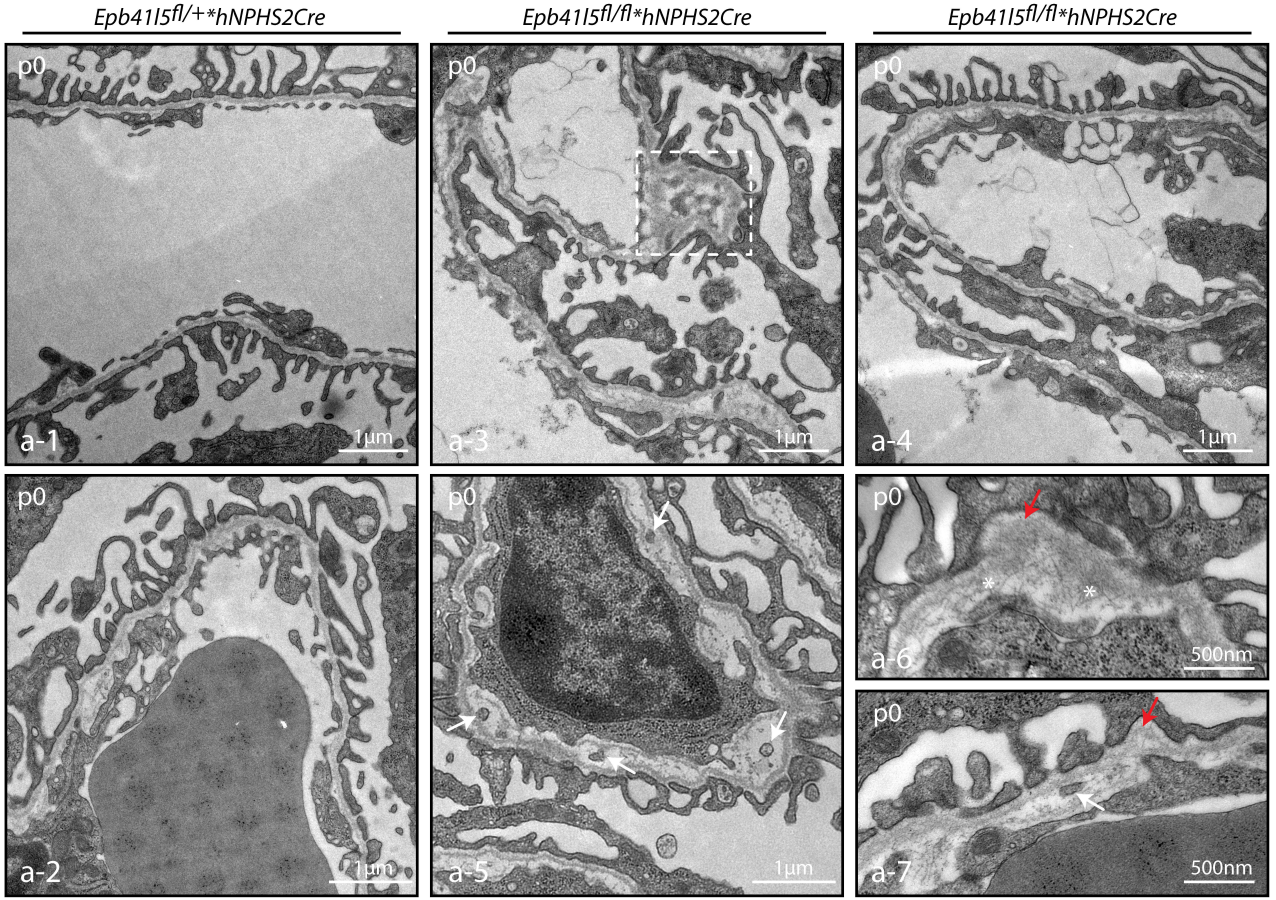

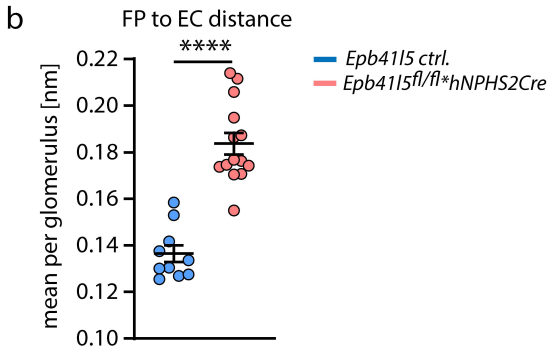

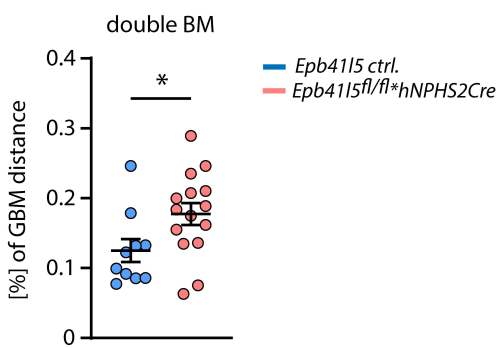

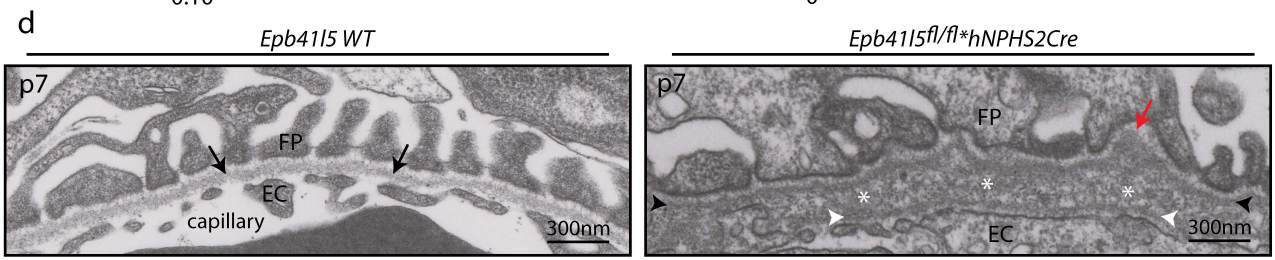

Supplemental Figure 3

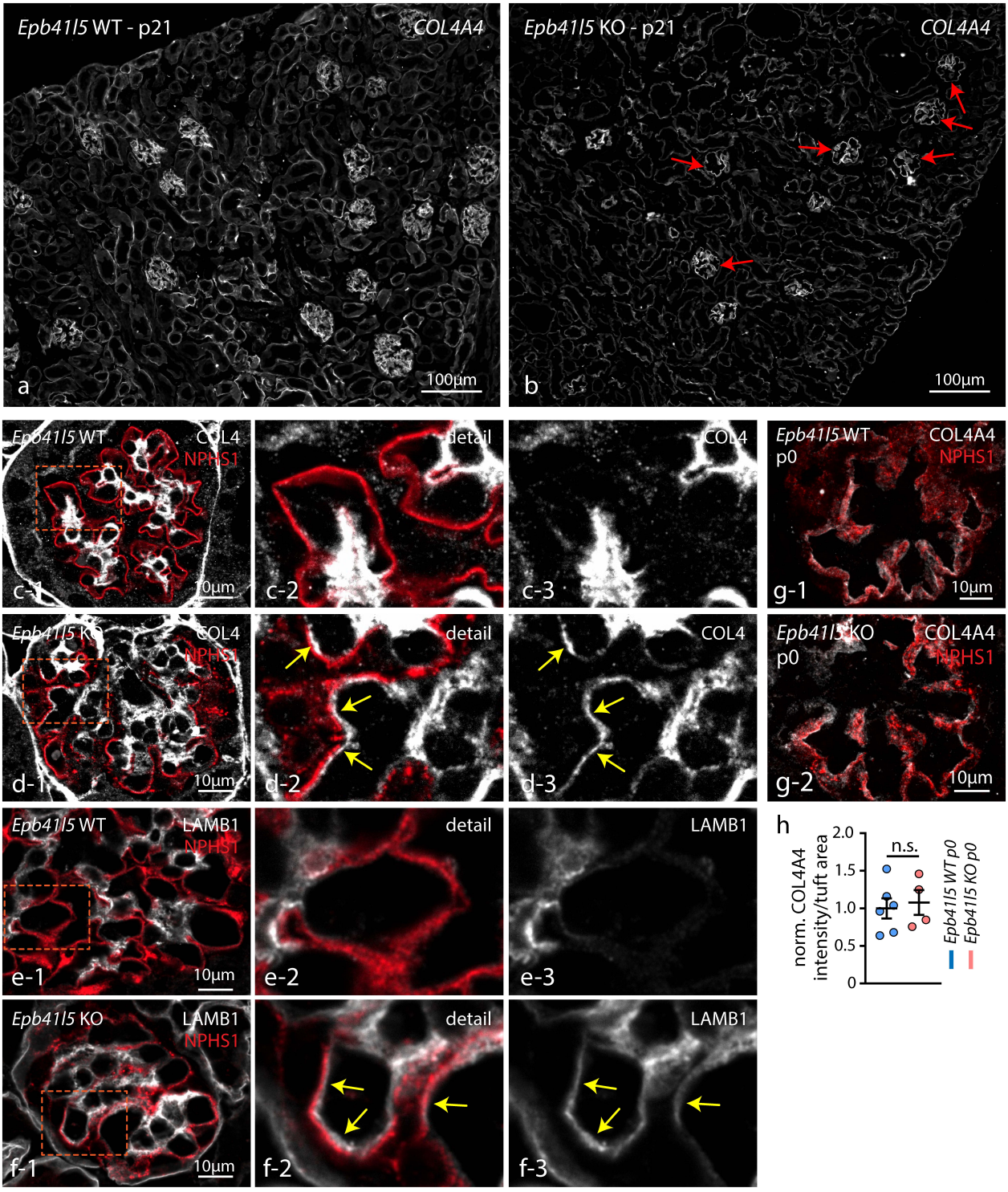

Supplemental Figure 4

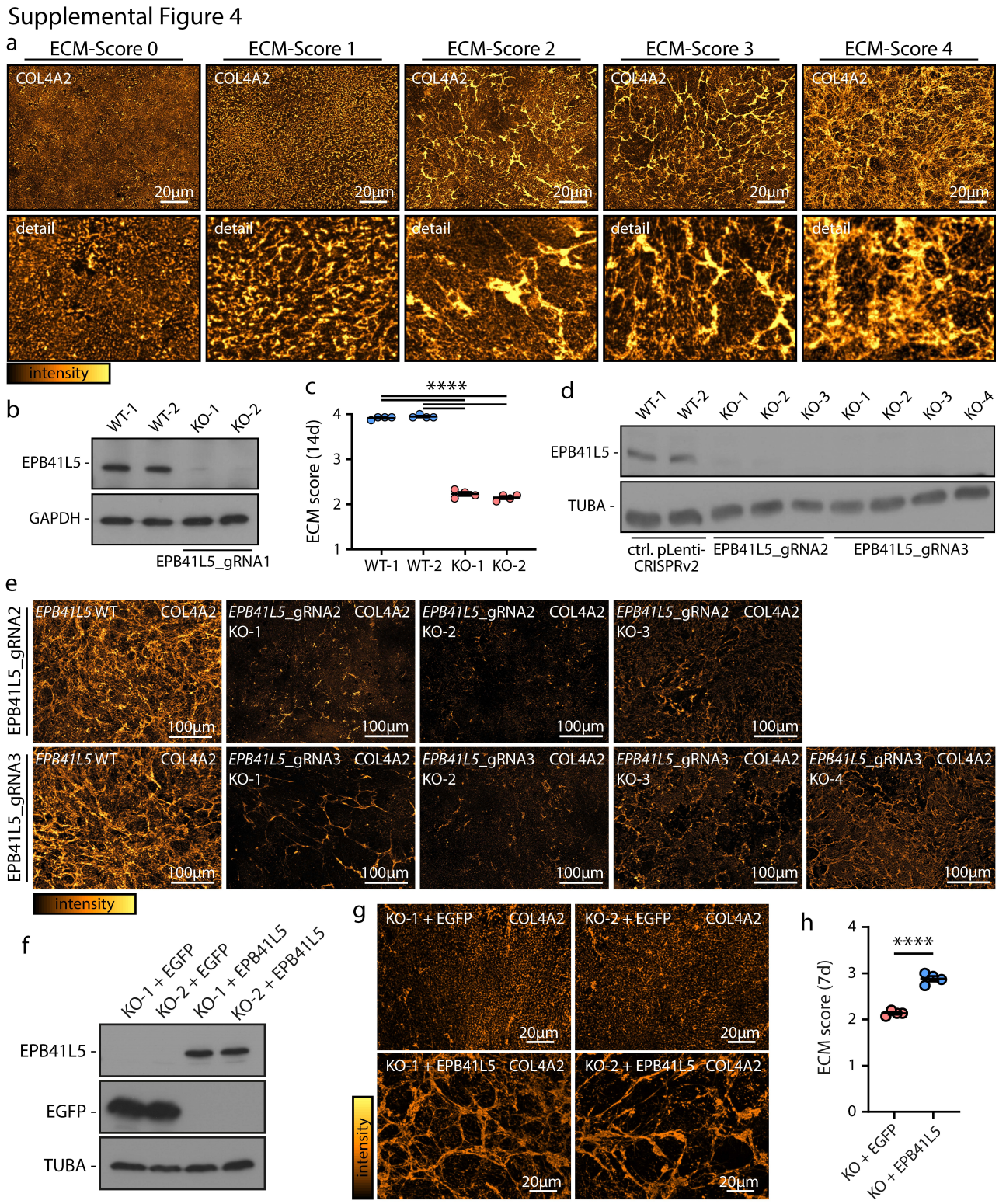

Supplemental Figure 5

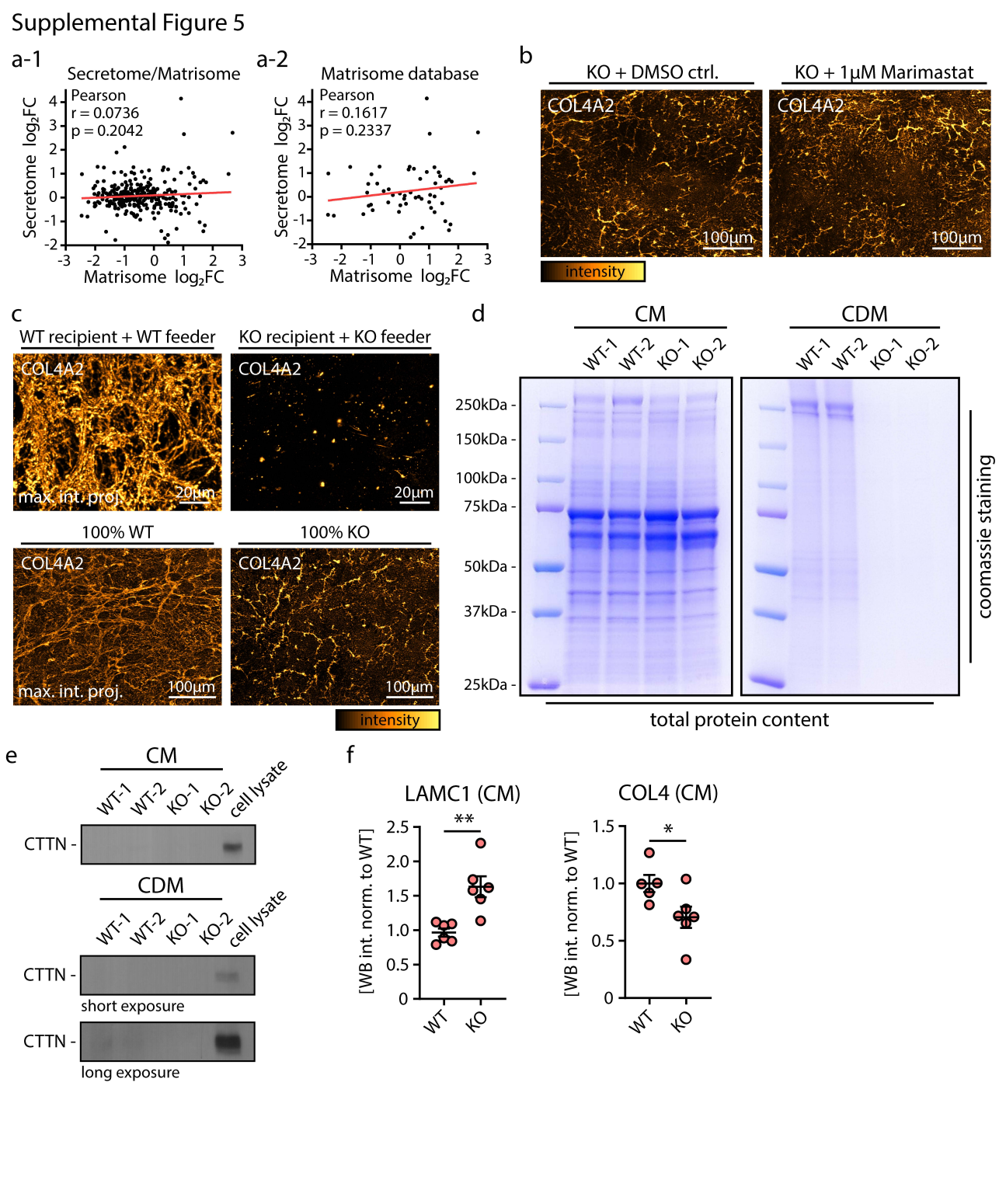

Supplemental Figure 6

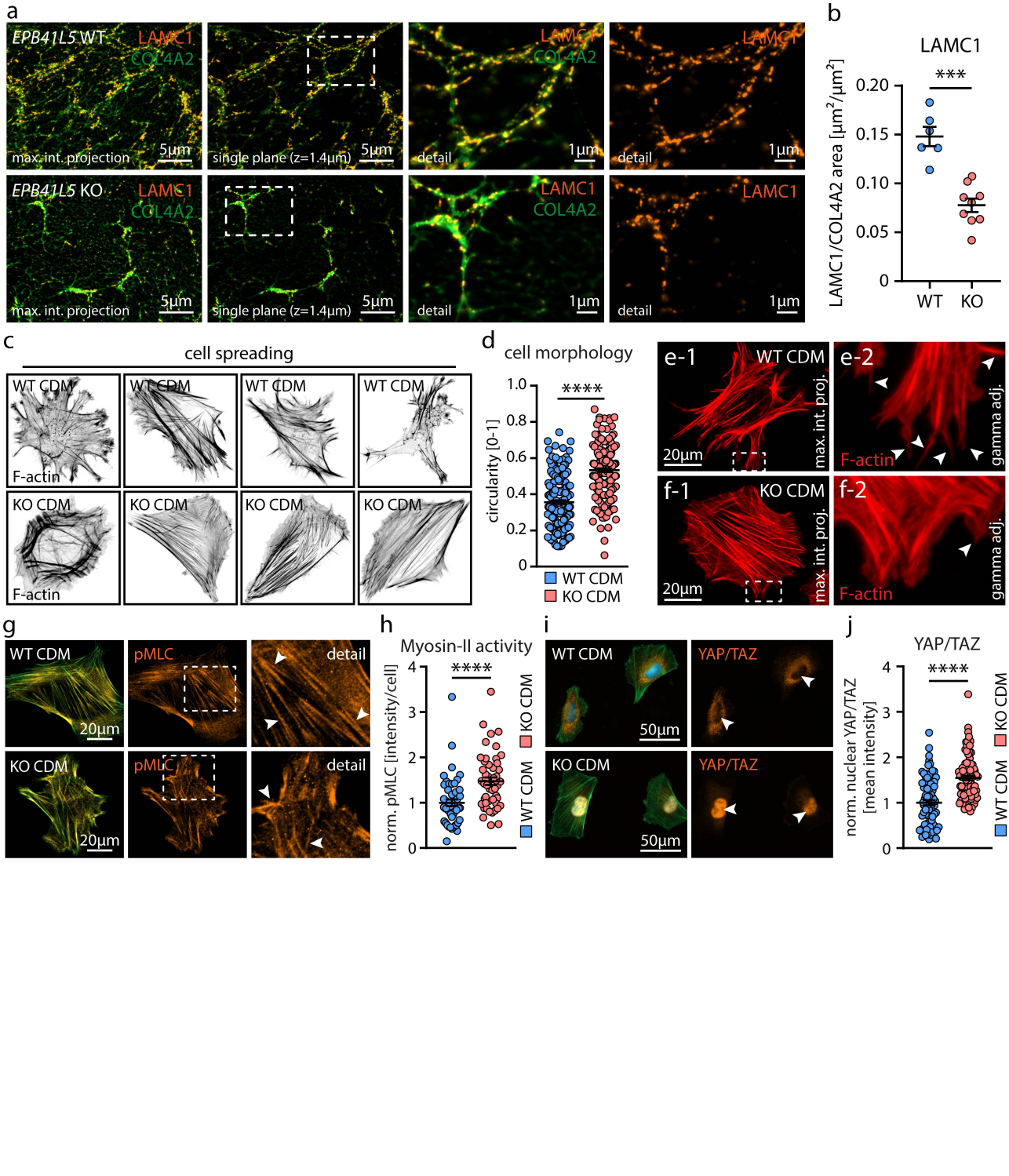

Supplemental Figure 7